International Journal of Thermal Sciences 228 (2026) 111009

Contents lists available at ScienceDirect

International Journal of Thermal Sciences

journal homepage: www.elsevier.com/locate/ijts

A research on melting, energy storage, and entropy generation in a vertical shell-tube latent heat storage system with different fin models and laminar flow regimes

Emrehan Gürsoy [a,b,*]

[a] Recep Tayyip Erdoğan University, Department of Energy Systems Engineering, Faculty of Engineering and Architecture, Rize, 53100, Türkiye
[b] Karabük University, Center of Energy Applications Laboratory, Karabük, 78050, Türkiye

ARTICLE INFO

Keywords:
Energy storage
Entropy generation
Laminar flow
Latent heat
Melting
Vertical shell and tube heat exchanger

ABSTRACT

This numerical study investigates the melting time, energy storage, and second-law efficiency of a latent heat thermal energy storage (LHTES) system consisting of a vertical shell and tube heat exchanger using aluminium metal foam (MF) and fins with different geometries. RT58 paraffin wax phase change material (PCM) was used as the heat storage material, and heat input to the system was provided by hot water flowing through the inner tube in a laminar regime (Re = 1000 and 2000) and T_{inlet} = 358 K. Rectangular, triangular, and parabolic fin models with the same total surface area were compared under different fin lengths. The analyses were carried out using the enthalpy-porosity approach and the Darcy–Brinkman–Forchheimer model. The results show that fin geometry and dimensions are decisive factors in PCM melting time, energy storage capacity, and entropy generation (EnG). While rectangular fins provided the shortest melting time, parabolic fins stood out with a more homogeneous melting profile and lower overall EnG performance. The best performance was obtained with the longest parabolic fin (P3) model. This model provided 4-19% lower thermal EnG compared to other geometries. Re = 2000 significantly shortened the full melting time of the PCM by increasing heat transfer compared to Re = 1000. The results show that the combined use of MF and fins in vertical shell and tube LHTES systems increases energy storage efficiency and reduces thermodynamic irreversibilities.

Nomenclature

A	surface area, [m^2]	T_S	solidus temperature, [K]
A_{rf}	total surface area of rectangular fin [m^2]	T_L	liquidus temperature, [K]
A_{tf}	total surface area of rectangular fin [m^2]	u	velocity component of x-direction, [m•s^{-1}]
A_{pf}	total surface area of rectangular fin [m^2]	v	velocity component of y-direction, [m•s^{-1}]
A_{mush}	mush zone constant, [kg•m^{-3}•s^{-1}]	W	width, [m]
b	Richardson extrapolation in GCI	y	fin spacing [mm]
c_p	specific heat, [J•kg^{-1}•K^{-1}]	Y	height, [mm]
C_F	inertial coefficient, [m^{-1}]	z	fin thickness [mm]
d_f	fiber diameter, [m]	***Greek symbols***	
d_k	characteristic length, [m]	β	liquid fraction
d_p	pore diameter, [m]	ω	pore density, [PPI]
$\vec{g}$	gravity, [m•s^{-2}]	ε	porosity, [−]

(*continued on next column*)

(*continued*)

ΔH	enthalpy variation, [kJ]	ρ	density, [kg•m^{-3}]
H_L	latent heat, [J•kg^{-1}]	δ	tortuosity coefficient, [−]
k	thermal conductivity, [W•m^{-1}•K^{-1}]	λ	ratio of ligament radius to ligament length [−]
k_{eff}	effective thermal conductivity, [W•m^{-1}•K^{-1}]	μ	dynamic viscosity, [kg•m^{-1}•s^{-1}]
K	permeability, [m^2]	γ	thermal expansion coefficient, [K^{-1}]
L_{rf}	length of rectangular fin, [mm]	∇	gradient operator
L_{tf}	length of triangular fin, [mm]	***Abbreviations***	
L_{pf}	length of parabolic fin, [mm]	*EnG*	entropy generation
N	mesh number	*GCI*	grid convergence index
p	pressure, [Pa]	*LHTES*	latent heat thermal energy storage
r_1	inner tube radius, [mm]	*LTE*	local thermal equilibrium

(*continued on next page*)

* Corresponding author:
E-mail address: emrehan.gursoy@erdogan.edu.tr.

https://doi.org/10.1016/j.ijthermalsci.2026.111009
Received 29 January 2026; Received in revised form 25 April 2026; Accepted 11 May 2026

(*continued*)

r_2	shell radius, [mm]	*MF*	metal foam
Re	Reynolds number	*MRE*	mean relative error [%]
S	GCI solution value	*PCM*	phase change material
t	time, [s]	*PPI*	pores per inch
T	temperature, [K]	*SIMPLE*	Semi-Implicit Method for Pressure Linked Equations
T_{inlet}	inlet temperature, [K]		

1. Introduction

Accelerating industrialization, population growth, and technological advancements are driving further increases in energy consumption. This highlights the sustainability of energy resources and the security of energy supply. The environmental impact and limited of fossil fuels have increased interest in renewable energy sources. However, the limited availability of these resources and their fluctuating production characteristics, while sources such as solar energy have a greater energy potential than humanity's immediate needs, have led researchers to find new solutions. In this regard, thermal energy storage (TES) systems play a crucial role in ensuring continuity by minimizing the effects of the time lag between energy supply and demand and in ensuring the use of energy when and where it is desired [1,2]. An analysis by Karakurt et al. [3] indicated that TES systems play a key role in ensuring the efficient integration of renewable energy sources into the global energy system.

The main methods used in TES systems are as follows: sensible heat storage, latent heat storage, and chemical heat storage. Among these methods, PCMs stand out because they store large amounts of heat at constant temperature, have high energy density, and offer efficient performance [4]. Other important advantages of using PCMs are that they minimize sudden temperature changes in energy storage and heat recovery processes and offer a more compact structure by reducing the volume and weight of TESs. Therefore, PCMs are critical, especially in balancing the heating and cooling loads of buildings [5]. However, it is well known that the low thermal conductivity of PCMs limits system performance and negatively affects system efficiency in energy storage and discharge processes. Therefore, various additives and structural improvements have been developed to eliminate this inherent disadvantage of PCMs and to increase the efficiency of TESs [6]. To overcome this limitation, the heat transfer enhancement techniques proposed in the literature can generally be divided into three main categories [7]: (i) passive methods, (ii) geometric modification methods, and (iii) hybrid approaches. Passive methods primarily aim to improve the effective thermal conductivity of the PCM without altering the system geometry, while geometric methods improve heat transfer by increasing the surface area through structural modifications such as fins. On the other hand, hybrid approaches combine multiple techniques to take advantage of their synergistic effects.

MFs are one of the innovative solutions that stand out in overcoming this fundamental problem. Using MFs in conjunction with PCMs, creating a composite medium, increases the thermal conductivity of the system, improving overall heat transfer performance. Borhani et al. [8] used PCM and MF composites to enhance the performance of thermoelectric generators, achieving an approximately 25% increase in electrical energy generated by MFs. Numerous field studies in the literature emphasize that MFs not only increase thermal conductivity but also reduce the temperature gradient of PCMs and improve performance by providing a more uniform distribution [9–13]. However, despite these advantages, the presence of MF can reduce the effective latent heat storage capacity due to the volume occupied by the solid matrix; this indicates a trade-off between increased thermal conductivity and energy storage density.

Another significant advantage of using MFs in LHTES systems is their increased heat transfer area. Thanks to their high porosity and large surface area, MFs increase the heat transfer surface with PCM, enabling faster phase changes in both heat storage and discharge processes. Thus, the system can easily manage the variable user supply/demand balance. In a study by Ghalambaz et al. [14], it was reported that the use of anisotropic MFs shortened PCM melting time by up to 24%. Kurşun et al. [15] observed that integrating copper (Cu) foam with porosity $\varepsilon = 0.85$ and 0.90 into the system, along with their geometric modification, shortened the melting time by approximately 17% and 14%, respectively.

The material selection of MFs also plays an important role in system performance. When Gürsoy et al. [16] examined the LHTES performance of aluminium (Al) and Cu foams at different ε and pore density (ω, PPI) values, they found that Cu foam, thanks to its high thermal conductivity, provided 60% more efficient heat transfer than Al foam and shortened the melting time by 28.2%. The researchers also noted that the use of a denser foam (lower ε) shortened the melting time by approximately 52%, and that the ω value did not have a significant effect on system efficiency. In a similar study, Zhang et al. [17] showed that the thermal conductivity of PCM increased by 3.7-fold and 12.5-fold, respectively, with the use of Cu and nickel foams. Yadav et al. [18] conducted a numerical investigation comparing the effect of MF and fin structure on a multi-tube heat exchanger LHTES. The researcher outlined that MF is more effective than fin structure by nearly 70% about melting time.

The addition of MFs inevitably reduces the PCM volumetric ratio and thus the theoretical latent heat storage capacity, while significantly increasing the effective thermal conductivity of the composite system. This improvement contributes to an accelerated phase-change mechanism, reduced thermal gradients, and improved heat-transfer homogeneity. As a result, the system exhibits a higher proportion of available stored energy and improved charge/discharge rates. Therefore, in practical applications, MFs improve effective energy density and thermal storage performance, especially under time-constrained operating conditions [19,20]. A study by Li et al. [21] indicated that MFs in PCMs are used in applications such as passive cooling systems, heat storage systems, and thermoelectric power generation. It was emphasized that the high thermal conductivity and latent heat storage capacity achieved with this technique minimize the heat source temperature and provide positive effects on thermal management time. Another advantage of using MFs in LHTES systems is that they maintain the system's structural integrity and increase shape stability. Zhang et al. [22] reported that shape-stabilized PCMs using MFs as porous supports eliminate leakage problems and increase the system's thermal conductivity. Furthermore, researchers emphasized that MFs maintain the mechanical stability of the system by eliminating volume changes that occur during the PCM's phase change process. Summarizing all these research results, it can be concluded that MFs solve the problem of low thermal conductivity in PCMs, accelerate energy storage and discharge processes, homogenize temperature distribution, increase system energy density, and ensure structural integrity. These results demonstrate that the use of MFs in LHTES systems is of great technical and economic importance and plays an indispensable role in improving system performance.

However, despite the significant advantages offered by PCM and MF composites, additional optimizations are needed to further enhance the system's heat transfer performance and optimize the energy storage process. In this regard, the use of fin structures plays a critical role in LHTES systems, increasing the heat transfer surface area and enabling faster and more efficient heat transfer to the PCM. These geometric enhancement techniques improve conductive heat transfer; however, their performance strongly depends on fin design, and non-uniform temperature distribution may occur in regions far from the heat transfer surfaces. In particular, the integration of fin structures into MF + PCM composite systems further improves both the heat transfer rate and the uniformity of the temperature distribution [23,24]. A key factor enabling this is the ease of application of MFs with hybrid heat transfer enhancement techniques and their synergistic combination with other methods [25]. Nedjem et al. [26] numerically investigated a triplex tube LHTES system using fins, MFs, and nanoparticles. The results showed that the combination of MFs and fins shortened the energy storage time

by approximately 80% compared to the combination of MFs and nanoparticles.

To overcome the individual limitations of passive and geometric enhancement methods, hybrid approaches have been developed by combining MF and fin structures. In recent years, hybrid systems using MF and fin structures have received increasing attention in the literature. These hybrid structures aim to maximize heat transfer performance and reduce the system cycle time by combining the advantages of both methods. In a study conducted by Joshi and Rathod [27], a 50% increase in the melting rate was found in a system using only fins, while this increase was 16% in a system using only MF. However, it was reported that MF performed 15% better than fins in terms of total cycle time. This result highlights the need for hybrid structures to be preferred in applications requiring both fast storage and high energy efficiency. Application areas of MF and fin hybrid structures include solar energy storage [28], waste heat recovery [29], electronics cooling [30], and integrated thermal management systems [26]. In this context, experimental and numerical analyses conducted by Ding et al. [31] showed that placing MF between adjacent fins reduces the melting time by approximately 25%. Du et al. [32] investigated the effects of MF and fin structures on LHTES system performance, both individually and synergistically. The results showed that using MF and fins alone reduced the melting time by approximately 80% and 47%, respectively, while using MF and fins together reduced the melting time by approximately 84%. Lu et al. [33] determined that MF and fin structures shortened the melting time by approximately 60% compared to non-enhanced case. Similarly, Mahdi et al. [34], who investigated the shell and tube LHTES system, found that fin-supported MFs increased the melting rate by 58% and 42% compared to using only MF and only fins, respectively.

Shell and tube heat exchangers are among the most preferred structures in LHTES systems. This is primarily due to their high heat transfer area, compact design, and ease of adaptation to different application requirements [35]. The use of PCMs in shell and tube heat exchangers increases energy efficiency, particularly in applications such as solar energy and waste heat recovery. For example, the PCM in solar water heaters stores the heat collected during the day, enabling a hot water supply even when sunlight is not available. In a study by Oudaoui and Faraji [36], the discharge processes of different types of PCMs in shell and tube systems were numerically investigated. They reported that the PCM can control the temperature of the supplied water depending on its storage capacity and that different PCM types improve the discharge time.

The use of shell and tube heat exchangers in LHTES systems not only increases the energy storage capacity but also enables the system to be more compact. In a study by Kudachi et al. [37], both experimentally and numerically, both heat storage and discharge cycles of a system containing an organic PCM mixture were tested. The results calculated that the energy change during the 100-min storage period was 458.2 kJ and the energy change during the 50-min discharge period was 316.0 kJ. The researchers stated that shell and tube heat exchangers offer effective heat storage and recovery opportunities. One of the most important advantages of PCM-based shell and tube heat exchanger systems is their ability to provide constant temperature heat transfer during energy storage and recovery processes, which is of great importance in industrial processes and comfort applications where temperature fluctuations are undesirable [38]. Shell and tube heat exchangers are also positioned vertically due to the facilitation of natural convection of the fluid passing through them, their smaller footprint, and ease of maintenance [39,40]. In addition, vertical configurations promote stronger natural convection effects, which significantly influence the melting behaviour of PCM.

Although shell and tube heat exchangers offer inherently positive performance factors, they suffer from the major drawbacks of PCM, such as its low thermal conductivity, when used as LHTES system. This has been addressed by many researchers in the literature [41–44]. To address this low thermal conductivity, optimization methods such as MF and fin structures, which are applicable to PCM, are being implemented. However, a search of the Scopus database using specific keywords reveals that MF-based studies on vertical shell and tube applications are relatively rare, while research on MF and fin structures is virtually non-existent. Numerical data and keywords related to this research are presented in Fig. 1. As shown in the figure, the number of studies examining the combined use of MF and fins in vertical tube systems is quite limited (2 records), which highlights the originality of the present study and is an important indication that it is open to further research.

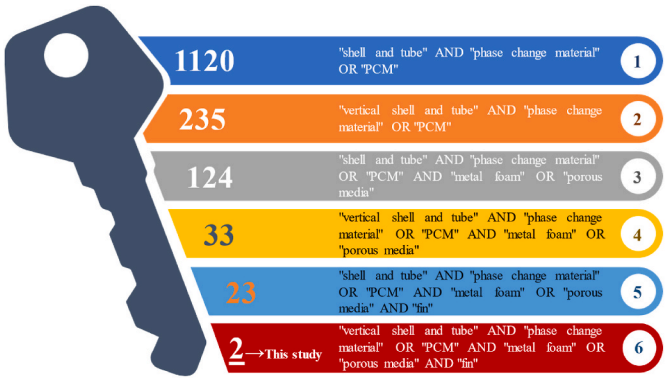

Fig. 1. Number of studies containing combinations of keywords "shell and tube", "vertical shell and tube", "phase change material/PCM", "metal foam/porous media", and "fin" in the Scopus database. The color intensity reflects the frequency of occurrence. It is clearly seen that while a large number of studies exist for conventional shell and tube PCM systems, the combination of vertical shell and tube, MF, and fin structures has been investigated in only a very limited number of studies (highlighted), indicating a significant research gap addressed in this study. (For interpretation of the references to color in this figure legend, the reader is referred to the Web version of this article.)

Despite the extensive research on PCM-based LHTES systems, previous studies have primarily focused on (i) the use of MF alone, (ii) fin-assisted configurations, or (iii) hybrid systems without systematic geometric comparison. In particular, most existing studies on shell and tube systems have considered horizontal configurations and conventional fin geometries such as straight or annular fins. Moreover, second-law (EnG) analysis has been largely neglected in hybrid MF-fin systems. To clearly highlight these research gaps, a comprehensive comparison of previous studies is presented in Table 1. As summarized, no prior study has simultaneously investigated (i) vertical shell and tube configuration, (ii) MF-fin hybrid enhancement, (iii) different fin geometries with equal surface area, and (iv) detailed EnG analysis. Therefore, the present study aims to fill this critical gap in the literature.

In this study, a vertical shell and tube heat exchanger is considered as an LHTES system, and straight fins with the same surface area and different shapes (rectangular, triangular, and parabolic) are placed in the tube geometry of system. A review of the literature reveals that in most studies on vertical shell and tube heat exchangers, the investigated fin structures generally have a flat shape [45–47], a Y-shape [48], a spiral shape [49], and a dendritic shape [50]. In summary, although MF and fin structures have been widely studied, their combined thermo-hydraulic and thermodynamic behavior in vertical shell and tube systems remains insufficiently explored, particularly with respect to EnG and geometric optimization. Therefore, this study not only fills a clear gap in the literature but also provides a systematic and comparative framework for the design of high-performance LHTES systems. RT58 PCM was chosen as the heat storage material in the system, falling between the shell and tube shapes. The heat input to the system is achieved by water flowing through the tube at a laminar flow condition with a Reynolds number (Re) of 1000 to 2000 and an inlet temperature of T_{inlet} = 358 K. With the help of the numerical results obtained, the optimum configuration was determined by taking into account the melting time, PCM melting profile and heat storage capacity.

Table 1
Comparison of the present study novelty with literature.

Study	Geometry	MF	Fin	Fin type	Vertical	EnG analysis	Key focus
Lu et al. [33]	Shell and tube	✔	✔	Straight	✔	X	Melting rate
Mahdi et al. [34]	Shell and tube	✔	✔	Straight	X	X	Heat transfer
Kudachi et al. [37]	Shell and tube	X	X	X	X	X	Energy storage
Strunga et al. [40]	Shell and tube	X	X	X	X	X	Heat transfer
Wołoszyn and Szopa [41]	Helical coiled shell and tube	X	✔	Spiral	✔	X	Heat transfer
Wu et al. [42]	Shell and tube	X	✔	Annular	✔	X	Heat transfer and energy storage
Chibani et al. [43]	Shell and tube	X	X	X	X	X	Heat transfer
Mao et al. [44]	Rectangular shell and tube	X	X	X	✔	X	Heat transfer
Present	Shell and tube	✔	✔	Rectangular, triangular, and parabolic	✔	✔	Thermodynamic, melting, energy storage, and EnG

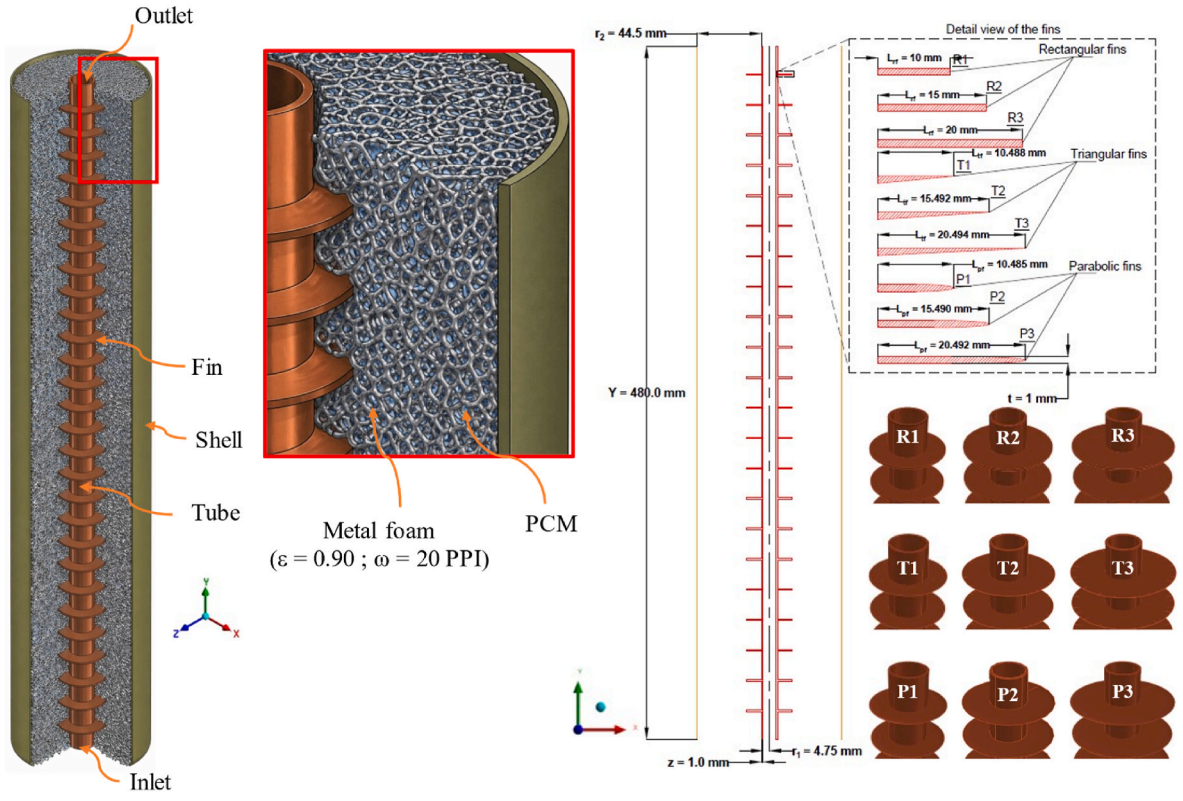

Fig. 2. Schematic presentation of the computational model.

Furthermore, this study provides a second-law (entropy-based) evaluation, which is rarely addressed in similar hybrid LHTES systems.

In addition to its scientific contribution, this study also offers significant practical implications for modern energy systems. LHTESs integrated with MF and optimized fin structures can be effectively used in various engineering applications such as solar thermal energy storage, waste heat recovery in industrial processes, thermal management of electronic devices, and energy-efficient building systems. In particular, improving melting performance and reducing EnG in these systems directly contributes to higher energy efficiency, lower operating costs, and increased system reliability. Therefore, the findings of this study not only provide fundamental information but also offer practical guidelines for the design and optimization of next-generation thermal energy storage systems.

2. Problem definition and methodology

2.1. Computational model description

The thermal model discussed in this study was analyzed in two-dimensional (2D) numerical approach. Although the actual geometry of the LHTES system is three-dimensional (3D), the geometry and boundary conditions are homogeneous along the axial direction. Furthermore, the fins are distributed periodically throughout the system. Therefore, the dominant heat transfer mechanisms occur primarily in the radial and vertical directions. In conclusion, similar studies in the literature appear to employ a 2D model to capture the fundamental thermal and flow characteristics of the system and significantly reduce computational costs [51,52].

Due to this the LHTES system, which consists of two vertically positioned concentric tubes, is presented in Fig. 2. The system consists of an inner tube with a radius of $r_1 = 4.75$ mm and a wall thickness of $z = 1$ mm, which carries water flowing under forced convection

Table 2
Visual presentation and geometric definition of the fins.

Fin type	Dimension equations [53]	Shape and dimensions of the fins
Rectangular	$L_c = L_{rf} + \frac{t}{2}$ $A_{rf} = 2wL_c$	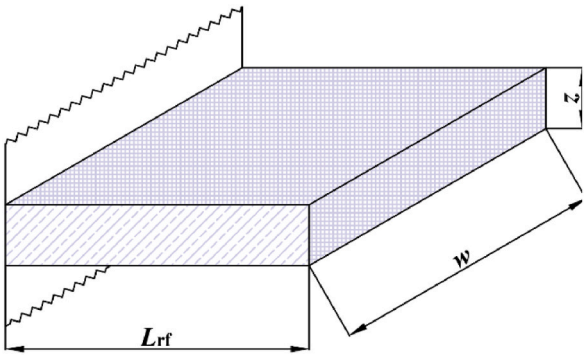
Triangular	$A_{tf} = 2w\sqrt{L_{tf}^2 + \left(\frac{t}{2}\right)^2}$	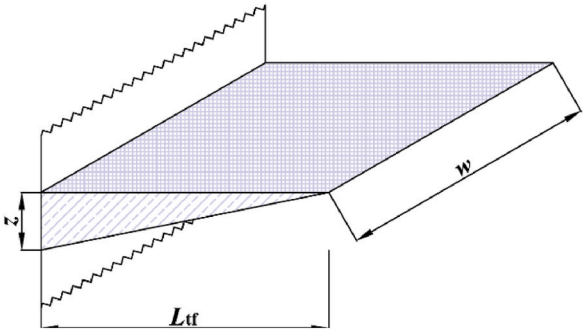
Parabolic	$A_{pf} = wL\left[C_1 + \left(\frac{L}{t}\right)\ln\left(\frac{t}{2} + C_1\right)\right]$ $C_1 = \sqrt{1 + \left(\frac{t}{L_{pf}}\right)^2}$	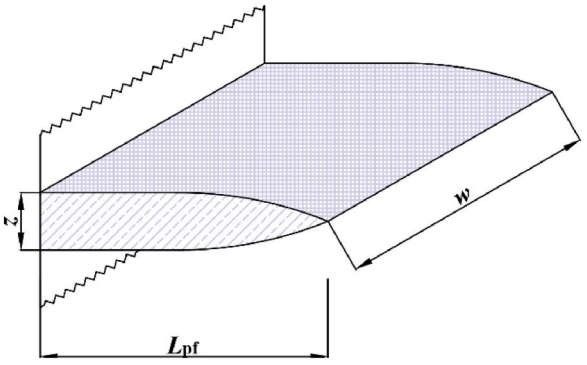

conditions, and a cylindrical shell geometry with a radius of $r_2 = 44.5$ mm. The system length is $Y = 480$ mm and is identical for both tubes. Twenty-two Cu fins with rectangular, triangular, and parabolic geometries, also with a thickness of $z = 1$ mm and a spacing of $y = 20$ mm, are installed in the inner tube. Detailed images and geometric characteristic formulations of these fins are also presented in Table 2. An RT58 PCM, capable of latent heat energy storage, is placed between the inner tube and the shell geometry, and an Al foam with properties of $\varepsilon = 0.90$ and $\omega = 20$ PPI is also placed in this section. Water flows through $+ y$ direction in the inner tube at flow conditions of Re = 1000 and 2000, and the inlet temperature of the water is $T_i = 358$ K. These flow regime values are typical for LHTESs to ensure laminar flow conditions. Instead of analysing turbulence effects, the aim of this study is to investigate the effects of fin geometry and MF on heat transfer and melting behaviour under controlled flow conditions. The water is assumed to flow to the atmosphere, and a boundary condition of $P_{outlet} = 0$ Pa is applied to the inner tube outlet. The shell geometry is assumed to be completely isolated from the environment, and that no heat transfer occurs (adiabatic). A no-slip boundary condition is applied at the points where both the water and the PCM come into contact with the tube, shell, and fin walls.

In the dimensioning operations for the fins, a rectangular fin structure was taken as the basis, and their lengths were determined as $L_{rf} = 10$, 15, and 20 mm. As a result of the calculations made with the equations $L_c = L + \frac{t}{2}$ and $A_{rf} = 2wL_c$, the total A_{rf} of all fins in the system was calculated as 0.146, 0.215, and 0.285 m^2, respectively. The surface areas of three different fin geometries are designed to be equal ($A_{rf} = A_{tf} = A_{pf}$). As a result of the reverse operations, the fin lengths of the triangular fin structure were calculated as $L_{tf} = 10.488$, 15.492, and 20.494 mm, respectively, while the fin lengths of the parabolic fin structure were determined as $L_{pf} = 10.485$, 15.490, and 20.492 mm, respectively.

In this study, the selection of fin geometries is based on both physical considerations and gaps identified in the literature. Three different fin structures (rectangular, triangular, and parabolic) were chosen to systematically investigate the effect of fin shape on heat transfer and melting behavior under the same surface area conditions. By maintaining an equal total surface area for all fin configurations, a fair comparison was ensured by separating the effect of the working geometry from the effect of the heat transfer area. The selected fin geometries enable a comprehensive comparison between conventional and less-explored designs, while also addressing a clear research gap in the

Table 3
Thermophysical properties of the materials.

Properties	RT58 [54]	Water [55]	Cu [56]	Al [56]
Density, ρ [kg•m^{-3}]	825	988.2	8900	2719
Specific heat, c_p [J•kg^{-1}•K^{-1}]	2000	4182	385	871
Thermal conductivity, k [W•m^{-1}•K^{-1}]	0.2	0.6	401	202.4
Dynamic viscosity, μ [kg•m^{-1}•s^{-1}]	0.0269	0.001003		-
Thermal expansion coefficient, γ [K^{-1}]	0.00011			-
Latent heat, H_L [J•kg^{-1}]	160000			-
Solidus temperature, T_S [K]	326			-
Liquidus temperature, T_L [K]	332			-

literature.

The basic thermohydraulic process in the system occurs as follows: when water enters the inner tube at high temperature, it undergoes both hydraulic and thermal development and begins to heat the tube wall. Over time, the heat reaches the PCM via the tube wall and fins. Melting begins when the PCM temperature reaches the solidification temperature (T_S), and melting ceases when all local temperatures reach the liquidus point (T_L). The thermophysical properties of the RT58 PCM, water, Cu, and Al materials used in the system are listed in Table 3. The main factors behind selecting RT58 as a PCM include its melting point, high energy density, and commercial availability [57]. The main criteria for selecting aluminium foam to increase the effective thermal conductivity of the system are that the material has high thermal conductivity, relatively low density, and a compact structure [58].

2.2. Governing equations

The Finite Volume Method was used to solve continuity, momentum, and energy equations. The phase change process was simulated via the enthalpy-porosity method in order to acquire better insight into the solid-liquid interface during melting [49]. Additionally, the Al foam placed in the PCM is analyzed using the Brinkman-Forchheimer extended Darcy model [59]. The local thermal equilibrium (LTE) approach was adopted for the heat transfer of the PCM and MF materials. Because pore-scale experimental and numerical studies show that the temperature difference between PCM and MF ligaments is negligible in many applications, this validates the LTE model [60,61]. In addition, some assumptions given below have been taken into account to simplify the solution process.

- There is no heat exchange between the solution geometry and its surroundings, and the phase change process occurs in an adiabatic environment.
- The thermophysical properties of PCM and Al foam are independent of temperature.
- There is no temperature difference between PCM and MF (based on the LTE approximation, $T_{PCM} = T_{MF}$).
- The liquid phases of water and PCM ($\beta = 1$) are assumed to be Newtonian and incompressible.
- The structure of the MF exhibits homogeneity in all directions, i.e., isotropic.
- At time $t = 0$, the system temperature is $T_{initial} = 298.15$ K.
- Since natural and forced convection are laminar flow regimes, viscous dissipation and radiative heat transfer are neglected.
- Due to the very low melting temperature range of 4 °C, the density is constant. However, the Boussinesq approximation is taken into account in the momentum equation to solve for the effect of buoyancy in natural convection.
- The thermal contact resistance between the fin structures and the Al foam is neglected.

The above assumptions are widely adopted in the numerical investigation of PCM-MF latent heat thermal energy storage systems and are considered reasonable for the operating conditions examined in this study. First, it is assumed that the thermophysical properties of PCM and Al foam are constant because the melting process of RT58 PCM occurs within a very narrow temperature range (4 °C). Under these conditions, the temperature variation of thermophysical properties has a negligible effect on the overall melting behaviour and heat transfer characteristics [62,63]. Second, the LTE assumption is used between the PCM and the MF skeleton. Due to the high thermal conductivity of the MF bonds and the very small pore size relative to the macroscopic dimensions of the system, the temperature difference between the PCM and the solid foam matrix is generally very small. Therefore, it can be assumed that both phases share the same temperature range; this significantly simplifies the energy equation while accurately representing the heat transfer mechanism reported in many previous studies [64]. Finally, the thermal contact resistance between the fin structures and the Al foam is neglected. In practical latent heat thermal energy storage systems, fins are typically manufactured as a tube-integrated structure or attached to a porous matrix using highly conductive bonding processes. Therefore, the contact resistance is significantly smaller than the overall conduction resistance within the PCM-MF composite, and its effect on the overall heat transfer behaviour is minimal [65].

As a result of the specified solution models and assumptions, the governing equations used in the analysis of melting, heat transfer, and flow movements for both natural and forced convections in the LHTES system are as follows.

Continuity equation for PCM melting and water flow [66]:

$$\frac{\partial \rho}{\partial t} + \nabla(\rho \vec{v}) = 0 \tag{1}$$

here, $\vec{v}$ [m•s^{-1}], ∇, and ρ [kg•m^{-3}] show the velocity vector, partial derivative combinations of x-y directions, and density, respectively.

Momentum equation for PCM melting [66]:

$$\frac{\rho_{PCM}}{\varepsilon}\frac{\partial \vec{v}}{\partial t} + \frac{\rho_{PCM}}{\varepsilon^2}\vec{v}\cdot\nabla\vec{v} = -\nabla p + \frac{\mu_{PCM}}{\varepsilon}\nabla^2\vec{v} + \rho_{PCM}\vec{g}\gamma\Delta T_0 + S_1 + S_2 \tag{2}$$

in this equation, ε, p [Pa], μ [kg•m^{-1}•s^{-1}], $\vec{g}$ [m•s^{-2}], γ [K^{-1}], and ΔT [K] symbolize the MF porosity, pressure, gravity (9.81 m s^{-2}), dynamic viscosity, thermal expansion coefficient, and temperature difference, respectively. Besides, $\rho_p \vec{g}\gamma(T - T_0)$ calculates the buoyancy force based on the Boussinesq approximation.

The source term S_1 is used to account for the resistance resulting from the decrease of porosity in the soft region during the phase change and is defined as in Eq. (3) [66]:

$$S_1 = -\frac{(1-\beta)^2}{(\beta^3 + 0.001)}A_{mush}\vec{v} \tag{3}$$

where A_{mush} [kg•m^{-3}•s^{-1}] is the mush zone constant (10^5 kg m^{-3} s^{-1} [67]), and 0.001 is a coefficient that prevents the equation from being divided by zero. Furthermore, β is the liquid fraction in the PCM and is determined according to Eq. (4) [66]:

$$\beta = \frac{\Delta H}{H_L} = \begin{cases} 0 & if\ T_{PCM} < T_S \\ \dfrac{T_{PCM} - T_S}{T_L - T_S} & if\ T_S < T_{PCM} < T_L \\ 1 & if\ T_{PCM} > T_L \end{cases} \tag{4}$$

in this equation, ΔH [J•kg^{-1}], H_L [J•kg^{-1}], and T [K] are the latent heat energy variation, the latent heat energy capacity, and temperature, respectively. Additionally, the subscripts PCM, S, and L refer to the

phase change material, the solidus temperature of the PCM, and the liquidus temperature of the PCM, respectively.

The source term S_2 is included in the main equation, as in Eq. (5), to account for the resistance due to the Al foam [66]:

$$S_2 = -\left(\frac{\mu_p}{K}\vec{v} + \frac{C_F}{\sqrt{K}}\rho_p \vec{v}|\vec{v}|\right) \tag{5}$$

here, K [m^2] and C_F [m^{-1}] define the permeability and inertial term.

Momentum equation for water flow [47]:

$$\rho_{water}\frac{\partial \vec{v}}{\partial t} + \rho_{water}(\vec{v}\cdot\nabla)\vec{v} = -\nabla p + \mu_{water}\nabla^2\vec{v} \tag{6}$$

Energy equation for PCM zone [66]:

$$(\rho c_p)_{eff}\left(\frac{\partial T}{\partial t} + V\cdot\nabla T\right) = k_{eff}\nabla^2 T - \varepsilon\rho_p H_L\frac{\partial \beta}{\partial t} \tag{7}$$

where c_p [J•kg^{-1}•K^{-1}] and H_L [J•kg^{-1}] represent the specific heat and latent heat, respectively. Furthermore, k_{eff} [W•m^{-1}•K^{-1}] symbolizes the effective thermal conductivity calculated with Eq. (8).

$$k_{eff} = \varepsilon k_{PCM} + (1-\varepsilon)k_{MF} \tag{8}$$

Energy equation for water flow [47]:

$$\rho_{water}c_{p_{water}}\left(\frac{\partial T}{\partial t} + \vec{v}\cdot\Delta T\right) = k_{water}\nabla^2 T \tag{9}$$

Additionally, conjugate heat transfer in the fins is calculated with the following equation [47]:

$$\rho_{Cu}c_{p_{Cu}}\frac{\partial T_{Cu}}{\partial t} = k_{Cu}\nabla^2 T \tag{10}$$

The energy stored in the melting of PCM including MF is calculated using following equations [66]:

$$H = \Delta H + h \tag{11}$$

$$\Delta H = \beta H_L \tag{12}$$

$$h = h_{ref} + \int_{T_{ref}}^{T} c_p dT \tag{13}$$

here h_{ref} [kJ.kg-1] shows the reference enthalpy, while T_{ref} [K] symbolizes reference temperature.

The local thermal ($\dot{S}'''_{gen,thermal}$), frictional ($\dot{S}'''_{gen,frictional}$), and total ($\dot{S}'''_{gen,total}$) EnG calculations were carried out by Eq. (14)–(16) [68]:

$$\dot{S}'''_{gen,thermal} = \frac{k}{T^2}\left[\left(\frac{\partial T}{\partial x}\right)^2 + \left(\frac{\partial T}{\partial y}\right)^2\right] \tag{14}$$

$$\dot{S}'''_{gen,frictional} = \frac{\mu}{T}\left\{2\left[\left(\frac{\partial U_x}{\partial x}\right)^2 + \left(\frac{\partial U_y}{\partial y}\right)^2\right] + \left(\frac{\partial U_x}{\partial y} + \frac{\partial U_y}{\partial x}\right)^2\right\} \tag{15}$$

$$\dot{S}'''_{gen,total} = \dot{S}'''_{gen,thermal} + \dot{S}'''_{gen,frictional} \tag{16}$$

2.3. Specifying metal foam characterization

To determine the viscous resistance and inertial resistance defined in the simulation program using the basic physical parameters of the Al foam, ε = 0.90 and ω = 20 PPI, the inertial coefficient, C_F [m^{-1}] calculated according to the Calmidi model [69] and the permeability, K [m^2] calculated according to the Du Plessis model [70] developed by Bhattacharya are given in Eqs. (17) and (18), respectively.

$$C_F = 0.00212(1-\varepsilon)^{-0.132}\left(\frac{d_f}{d_p}\right)^{-1.63}\begin{cases} d_p = \dfrac{0.0254}{\omega} \\ d_f = 1.18 d_p\sqrt{\dfrac{1-\varepsilon}{3\pi}}\left(\dfrac{1}{1-e^{\left(-\frac{1-\varepsilon}{0.04}\right)}}\right) \end{cases} \tag{17}$$

$$K = \frac{\varepsilon^2 d_k^2}{36(\delta^2-\delta)}\begin{cases} d_k = \dfrac{\delta}{3-\delta}d_p \\ \delta = 2 + 2\cos\left[\dfrac{4\pi}{3} + \dfrac{1}{3}\cos^{-1}(2\varepsilon - 1)\right] \end{cases} \tag{18}$$

here, d_f [m] is fiber diameter, d_p [m] is pore diameter, d_k [m] is characteristic length, and δ is tortuosity coefficient.

2.4. Numerical methods

In this study, thermal energy storage and flow characteristic analyses of the models under investigation were performed using ANSYS Fluent 2024 R1. The Finite Volume Method was used to solve the continuity, momentum, and energy equations in integral form over each volume. The melting characteristic of the PCM was solved using the enthalpy-porosity approach, representing the temperature-dependent liquid fraction and the solid and liquid regions. Furthermore, the Darcy-Brinkman-Forchheimer model was used to solve the Al foam structure placed between the tube and shell structures. For pressure-velocity matching and pressure correction, the SIMPLE algorithm and the PRESTO! scheme were used, respectively. Additionally, the second-order upwind scheme was chosen for the discretization of the momentum and energy equations. The continuity, momentum, and energy equations were approximated to values of 10^{-6}, 10^{-5}, and 10^{-6}, respectively, and for this purpose, the under-relaxation factors for pressure, momentum, energy, and fluid fraction were set to 0.3, 0.7, 0.9, and 0.8, respectively.

2.5. Grid convergence index and time step size sensitivity analyses

One of the most important issues in numerical time-dependent analyses is conducting mesh convergence and time-step size sensitivity analyses to achieve an optimal solution time and avoid high computational costs. In this context, a Grid Convergence Index (GCI) analysis [71] was performed on the liquid fraction results obtained from three different mesh intensities-coarse (N_1 = 89918), medium (N_2 = 237818), and fine (N_3 = 812942)-to determine the optimal mesh size required for the solutions. Small mesh structures, formed using Finite Volume Methods, were selected as tetrahedron, and inflation layers were used to improve the fluid and PCM solutions near the walls. Local mesh settings were utilized, considering orthogonal and skewness mesh quality indicators when forming these structures. The necessary solutions for the GCI analysis were performed in an R3 fin structure model at a flow regime of Re = 1000 and a time-step size of t = 0.5 s. According to method correlations, the improvement ratios for the relevant mesh sizes were found to be r_{21} = 1.626 and r_{32} = 1.849. The liquid fraction at t = 680 s, chosen as the solution size, was found to be S_1 = 0.931, S_2 = 0.959, and S_3 = 0.978 for three different meshes, respectively. The convergence order calculated according to Richardson extrapolation is b = 0.706. This value, which indicates small GCI values and small variations between successive mesh solutions, shows that the numerical results have a weak sensitivity to mesh refinement. In addition, the GCI values calculated for fine-medium and medium-coarse meshes were determined as GCI_{21} = 0.0682 and GCI_{32} = 0.0433, respectively. The control parameter is approximately 1.88%. The obtained results show that the numerical solution becomes mesh-independent and the discretization error is negligible. All liquid fraction results of the GCI

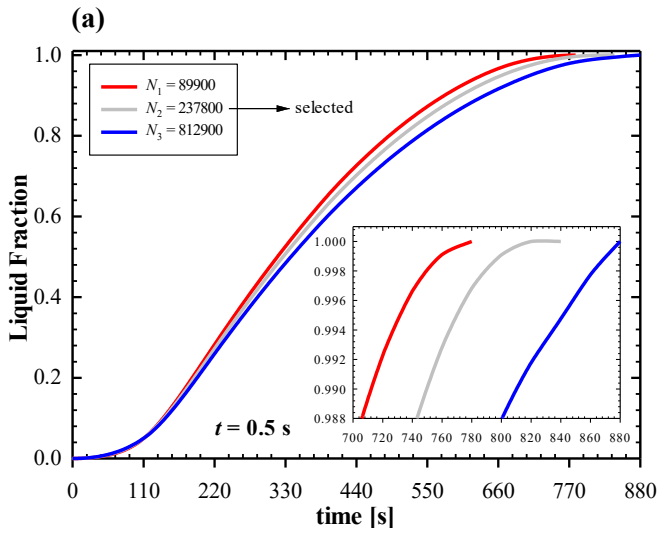

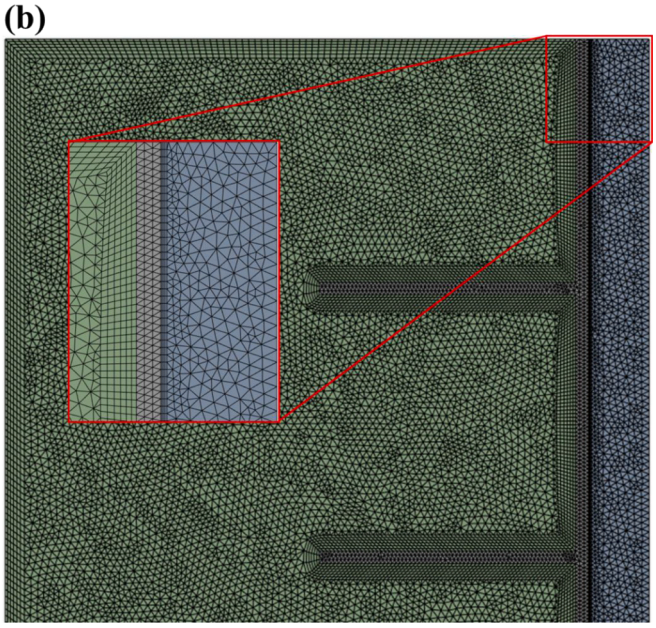

Fig. 3. Mesh number effect analysis of the LHTES model: (a) liquid fraction results at time step size of $t = 0.5$ s and Re = 1000, (b) presentation of optimum mesh ($N_2 = 237818$) structure.

analysis are presented in Fig. 3(a), and no significant difference was observed between different mesh sizes. The numerical results present that main relative error (MRE) was realized as 1.4% between $N_1 = 89918$ and $N_2 = 237818$. Also, this analysis indicated it as 2.3% between $N_2 = 237818$ and $N_3 = 812942$. Therefore, the medium mesh structure ($N_2 = 237818$) was preferred in subsequent analyses, and the relevant mesh structure is shown in Fig. 3(b) for rectangular finned LHTES system. The quality values of the obtained mesh structure were measured as follows: maximum skewness 0.726 and minimum orthogonal quality 0.384. These values are within the appropriate range for a computational fluid dynamics analysis model to perform calculations reliably, as confirmed by studies in the literature [72,73].

In time-dependent analyses, the time step size is a fundamental parameter that directly affects both solution accuracy and numerical stability, and is of great importance for reliable and efficient analysis. Excessively large time steps can lead to numerical instabilities and serious solution errors, while excessively small-time steps increase computational costs. Therefore, in this study, analyses were performed for an R3 fin structure model with $N_2 = 237,818$ mesh elements using

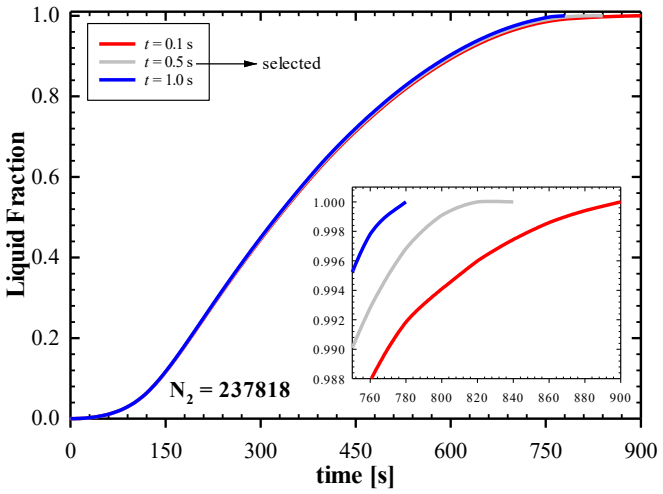

Fig. 4. Time step size effect on the liquid fraction in the LHTES model at $N_2 = 237818$ mesh structure and Re = 1000.

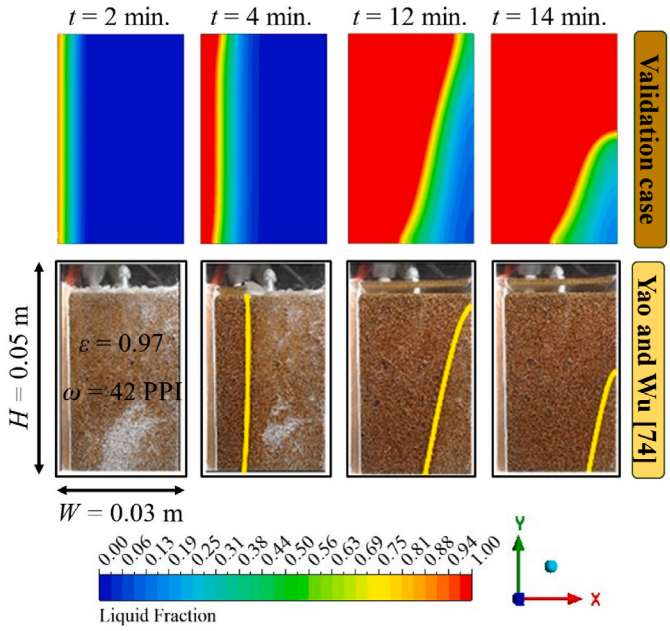

Fig. 5. Validation of the numerical procedure via liquid fraction.

different internal time step values ($t = 0.1$ s, 0.5 s, and 1.0 s), and the results obtained are presented in Fig. 4. The numerical results show that MRE was realized as 0.5% between $t = 0.1$ s and $t = 0.5$ s, while it realized as 0.5% between $t = 0.5$ s and $t = 1.0$ s.

2.6. Validation of the numerical setup

In the numerical model, mesh settings and solution methods were first validated by comparing them with experimental data from Yao and Wu's [74] experimental study on liquid fraction solid-liquid interface progression and temperature measurements. Thus, the reliability of the enthalpy-porosity method and the applied analysis techniques considered in the PCM melting process was proven. For this purpose, a vertical rectangular cavity with a height of $H = 0.05$ m and a width of $W = 0.03$ m was designed, filled with paraffin wax, and defined as Cu foam ($\varepsilon = 0.97$ and $\omega = 42$ PPI). In the case under investigation, a constant heat flux of $q" = 4000$ W m^{-2} was applied to the left wall, while the other surfaces were assumed to be adiabatic. It was determined that

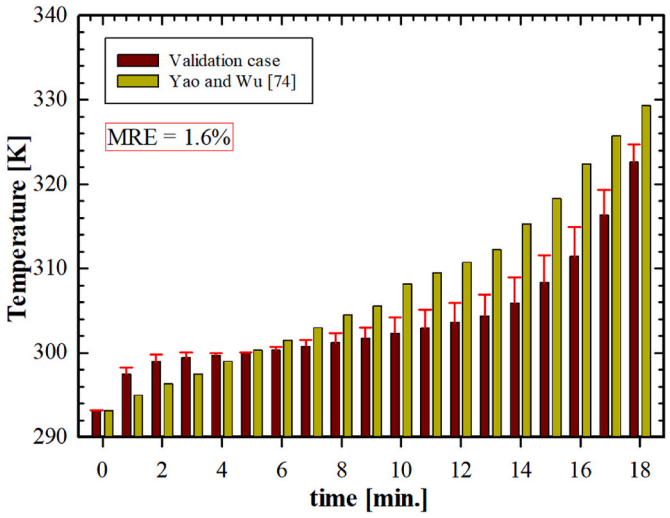

Fig. 6. Validation of the numerical procedure via PCM temperature variation over time.

the progression of the solid-liquid interface over time, given in Fig. 5, showed a high degree of similarity. In addition, it was determined that the time-dependent average PCM temperature change shown in Fig. 6 was also consistent with the experimental results. The mean relative error (MRE) between trends was calculated as 1.6%. The numerical model adopted for the current geometry has been validated and found to be in good agreement with well-known experimental data in the literature. This confirms the reliability of the numerical approach applied to predict the melting behaviour of PCM.

In addition to the validation study, the overall numerical uncertainty of the current model was assessed through grid convergence and time step size sensitivity analyses. The results showed that the average relative error remained in the range of approximately 1-2%. Therefore, differences below this range may fall within the numerical uncertainty band and should not be considered significant. Instead, the reliability of the results is supported by consistent trends observed in melting properties, EnG, and thermal behaviour.

3. Results and discussion

3.1. Effect of fin types and dimension

Fig. 7 shows the time-dependent liquid fraction evolution of nine different fin models in the Re = 1000. Although all fin geometries generally exhibit similar melting characteristics, it appears that fin shape and dimensions have significant effects on the melting rate. The phenomenon of a decrease in melting time with increasing surface area has also been observed in other studies in the literature [75,76]. When comparing the rectangular fin models in Fig. 7(a), it was calculated that R3 melted 1.7% and 0.12% earlier than R1 and R2, respectively. When comparing the triangular fin models in Fig. 7(b), it was observed that T3 melted 2.1% and 1.6% faster than T1 and T2, respectively. When a similar comparison was made for parabolic fin models, P3 melted 2.7% and 0.6% faster than P1 and P2, respectively, based on Fig. 7(c).

As shown in Fig. 7(d), among the models studied, rectangular fins

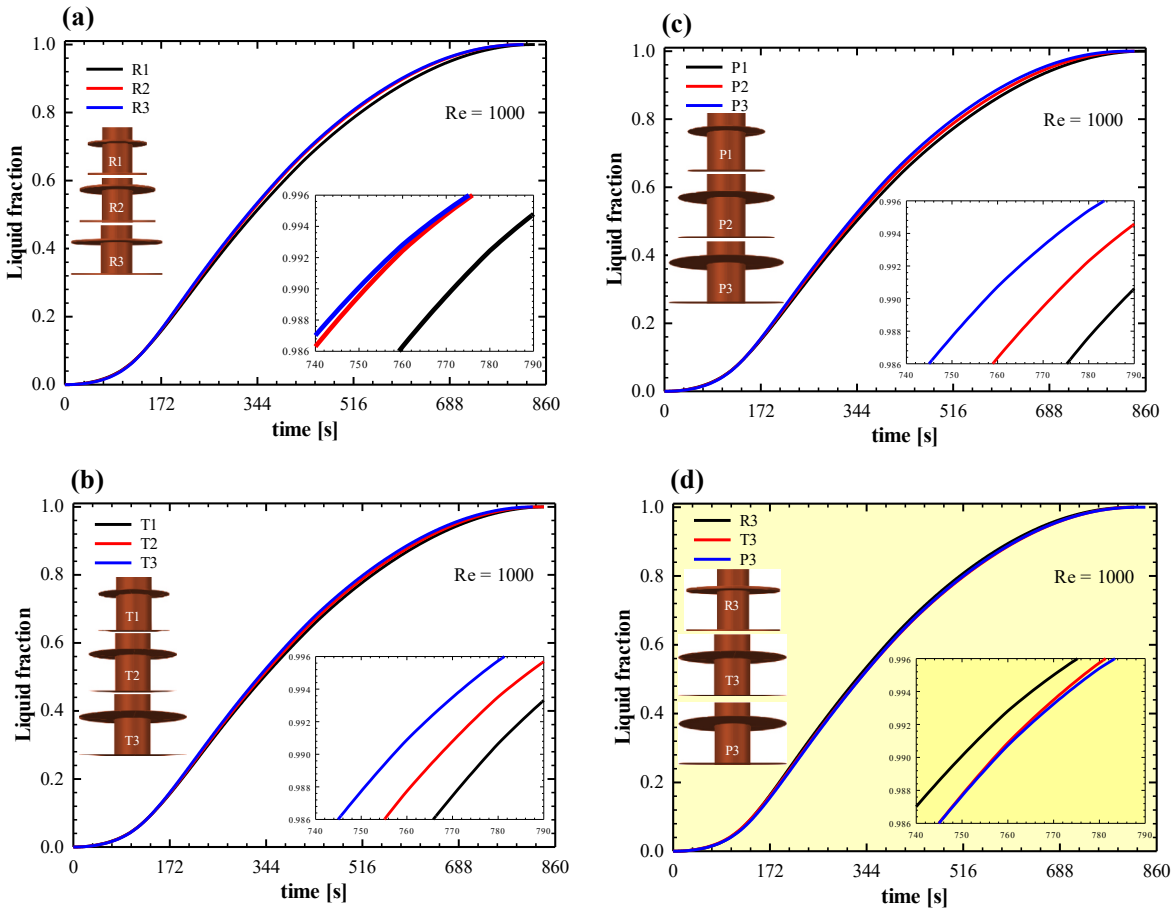

Fig. 7. Time-dependent PCM melting characteristic occurred in; (a) rectangular fin geometry, (b) triangular fin geometry, (c) parabolic fin geometry, and (d) best geometries.

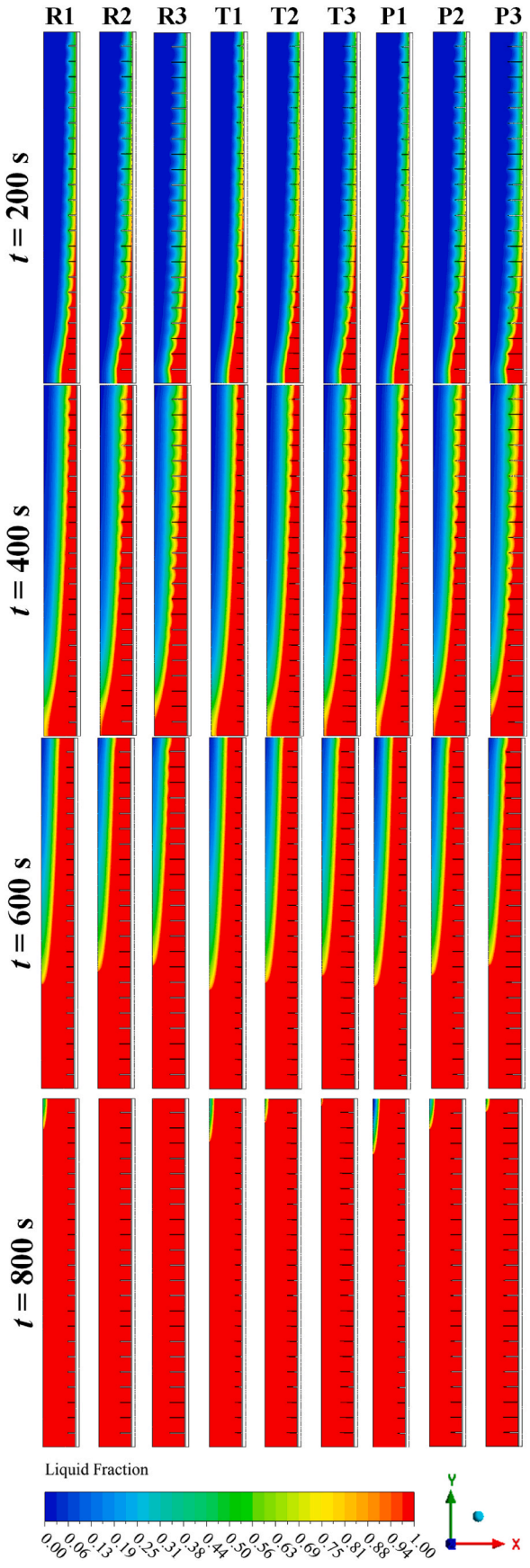

Fig. 8. Time-dependent PCM melting contours.

show the fastest melting behaviour, followed by triangular and parabolic fins. This behaviour mainly due to the more uniform heat transfer distribution provided by rectangular fins, which enhances conduction-dominated heat transfer [77]. In triangular and parabolic shapes, the area narrows towards the apex, so the effective heat transfer area decreases, which can slow down melting, especially in regions close to the fin tip [78]. The times when the PCM in the model reaches the full melting state ($\beta = 1$) are $t = 808$ s in the R3 model, whereas this time increases by 0.25% and 1.86% for T3 ($t = 810$ s) and P3 ($t = 823$ s) models, respectively. It is also observed that melting occurs faster as the fin radius increases. This is because, in materials such as PCM, where the heat transfer mechanism occurs through both conduction and convection, the surface area has a directly proportional effect on the heat transfer in the system according to the Fourier Law of Heat Conduction and Newton's Law of Cooling equations [53].

The time-dependent liquid fraction variations of the models are also shared as contours in Fig. 8. When the solid-liquid interface progressions are examined, it is observed that the high-temperature water in the $+y$ direction first melts the PCM at the lower right point of the cavity and progresses towards the upper left corner. The reason for the higher melting rate recorded at the inlet point of the fluid is related to the thermal and hydrodynamic behaviour of the water at inner tube inlet. The fluid has not developed thermally or hydrodynamically here, meaning that the velocity and temperature boundary layers are newly formed on the wall and are very thin. This causes a large temperature gradient to form between the wall and the fluid, and therefore high heat transfer to occur. As the flow progresses, both boundary layers thicken and the temperature gradient decreases [79,80]. On the other hand, small variations observed in the trends are also relatively noticeable in these contours, and it is seen that more PCM reaches the liquid phase as the fin area increases (from model coded as 1 to 3). When the colour distributions at $t = 800$ s were examined, it was understood that the R2 and R3 models reached the $\beta = 1$ condition and that the most solid PCM was present in the P1 model.

In the numerical study, the energy storage performances of nine different models were also examined, and the results for all models for the period up to the condition $\beta = 1$ are presented in Fig. 9. When the graphs are examined, it is observed that the energy change in PCM increases relatively as the surface area increases in three different fin models. In other words, even though the amount of PCM decreases as the fin surface area increases, it causes a larger portion of the PCM to completely melt in a unit time, thanks to the improvement in heat transfer, and this encourages the increase of the total stored energy [81]. When the numerical data in Fig. 9(a) are examined, the thermal energy stored by the R3 model is 0.44% and 0.25% higher compared to R1 and R2, respectively. In Fig. 9(b), the storage performance of the T3 model is 0.28% higher than the T1 model and 0.1% higher than the T2 model. In Fig. 9(c), the P3 model exhibited 0.71% and 0.67% higher energy storage performance compared to the P1 and P2 models, respectively. Finally, when comparing the different fin geometries showing the highest energy storage capacity in the relevant models in Fig. 9(d), it was determined that the P3 model stored 0.51% more energy than the R3 model and 1.10% more energy than the T3 model. Although the differences in stored energy between the models remain below 1%, these variations fall within the numerical uncertainty range of the present study. Therefore, performance evaluation is primarily based on EnG and melting behaviour rather than absolute energy differences. The improvement in energy storage is related to the increased homogeneity of the melting process and the reduction in local thermal resistance. Therefore, the main advantage of the P3 model lies not in maximizing the amount of stored energy, but in its ability to increase thermodynamic efficiency.

The study also examined effect of the fin geometries and dimensions on PCM EnG. Although EnG analysis was performed due to both the PCM melting process and the water flowing through the inner tube, the results presented do not include those related to water. This is because the

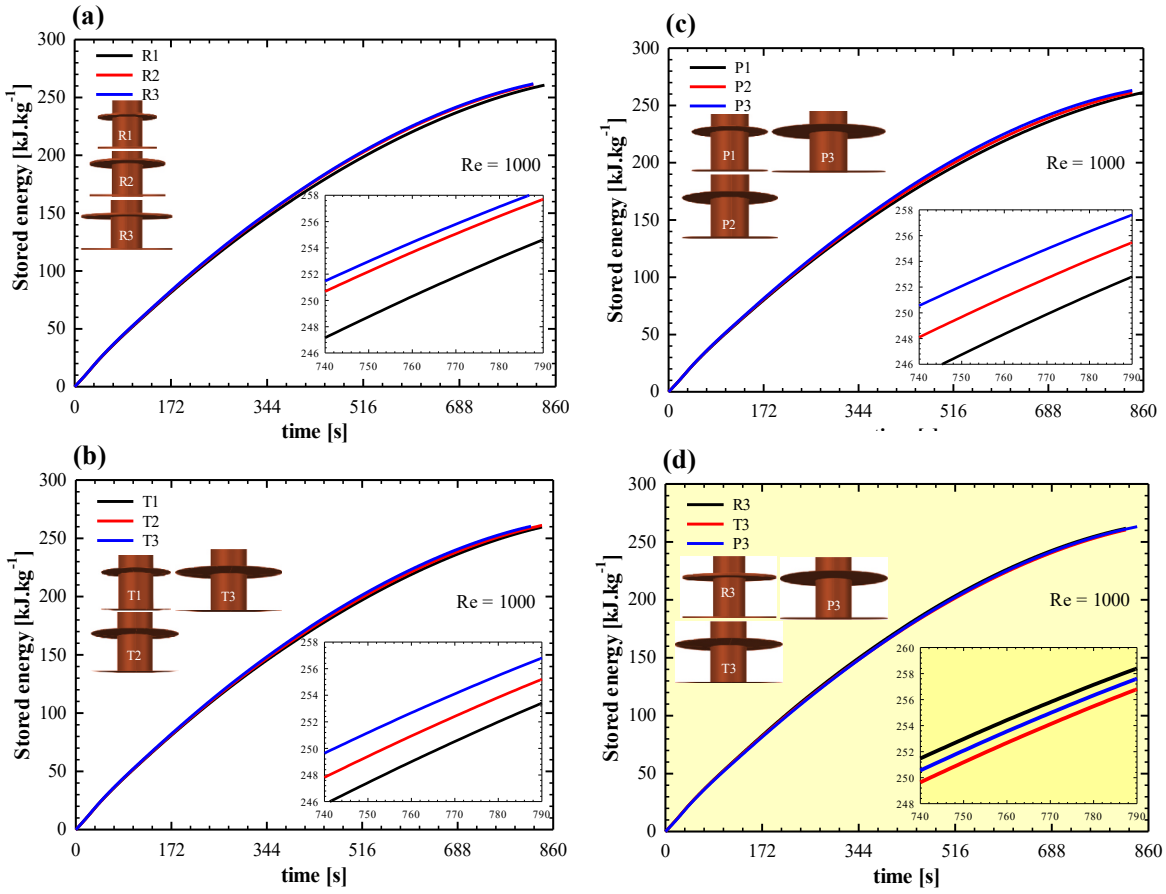

Fig. 9. Time-dependent PCM energy storage characteristic realized in; (a) rectangular fin geometry, (b) triangular fin geometry, (c) parabolic fin geometry, and (d) best geometries.

boundary conditions for water are identical in each model and do not show any change. EnG analysis provides important information about the thermodynamic performance of the LHTES system by identifying the dominant sources of irreversibility in the melting process. Based on this, the thermal EnG results related to the PCM melting process, along with the average temperature variation over time, are shared in Fig. 10. Upon examining all models, it is observed that there are abrupt changes and fluctuations in time-dependent irreversibilities. Since PCM is in the solid phase at the beginning of the process, heat transfer in the system occurs by conduction. On the other hand, the temperature difference between water and solid PCM is relatively large, leading to high thermal irreversibility. Due to the high gradients, a sudden increase in thermal EnG was observed in the first time period of approximately $t = 40$ s. The applied heat is more easily transferred to the PCM thanks to the MF. The average temperature of the material reaches the T_S value at approximately $t = 190$ s, and irreversibility tends to decrease between 40 s $< t <$ 190 s. The shaded region between T_S and T_L represents the phase change interval of the PCM, enabling a direct correlation between the melting process and EnG. As the average temperature enters this region, the coexistence of solid and liquid phases intensifies temperature gradients near the moving interface, which explains the observed variations in thermal EnG. However, beyond this point, molecular disorder increases as all the PCM in the system melts, and heat transfer in this process occurs based on finite temperature differences. Therefore, a non-stable phase boundary forms as the PCM melts; the temperature gradient is highest around this region, and heat conduction is intense and consequently, thermal EnG increases [82]. When the process reaches $t = 400$ s, the average temperature of the PCM reaches T_L, at which point reversibility becomes stationary and begins to decrease. Finally, the thermal EnG tends to decrease until all the PCM reaches the $\beta = 1$.

The presence of fins significantly affects the distribution of EnG within the PCM region. Fins increase heat transfer from the inner tube to the PCM and improve heat diffusion throughout the storage unit. As a result, the temperature field becomes more homogeneous, and local temperature gradients decrease. This leads to a reduction in thermal EnG compared to configurations with less effective heat dissipation capabilities. Therefore, fin geometries that provide a more uniform melt front generally exhibit lower thermal irreversibility. Consequently, when the effect of fin size differences on thermal EnG is examined, it is clearly seen that increasing the fin surface area has a positive effect on the irreversibility of the system. Examining the results in Fig. 10(a), it was observed that the R3 model caused 29% and 13% less irreversibility compared to R1 and R2, respectively. In Fig. 10(b), it was determined that the T3 model caused 18% and 7% less thermal EnG compared to the T1 and T2 models, respectively. In Fig. 10(c), P3 caused 29% less irreversibility compared to P1 and 14% less compared to P2. According to Fig. 10(d), the parabolic fin model was determined to have lower irreversibility compared to the others. Numerical results show that the melting process in P3 resulted in 4% less thermal EnG compared to R3 and 19% less compared to T3.

The contours obtained for time-dependent thermal EnGs are presented in Fig. 11. When the images are examined, it is understood that the thermal irreversibilities occurring in PCM exhibit a trend similar to that of liquid fraction. This is because high temperature gradients increase heat transfer and also act as a mechanism that triggers thermal irreversibilities. However, as PCM transforms into the liquid phase, especially after $t = 600$ s, the local temperature change becomes minimal, so it is observed that thermal irreversibilities are at their minimum

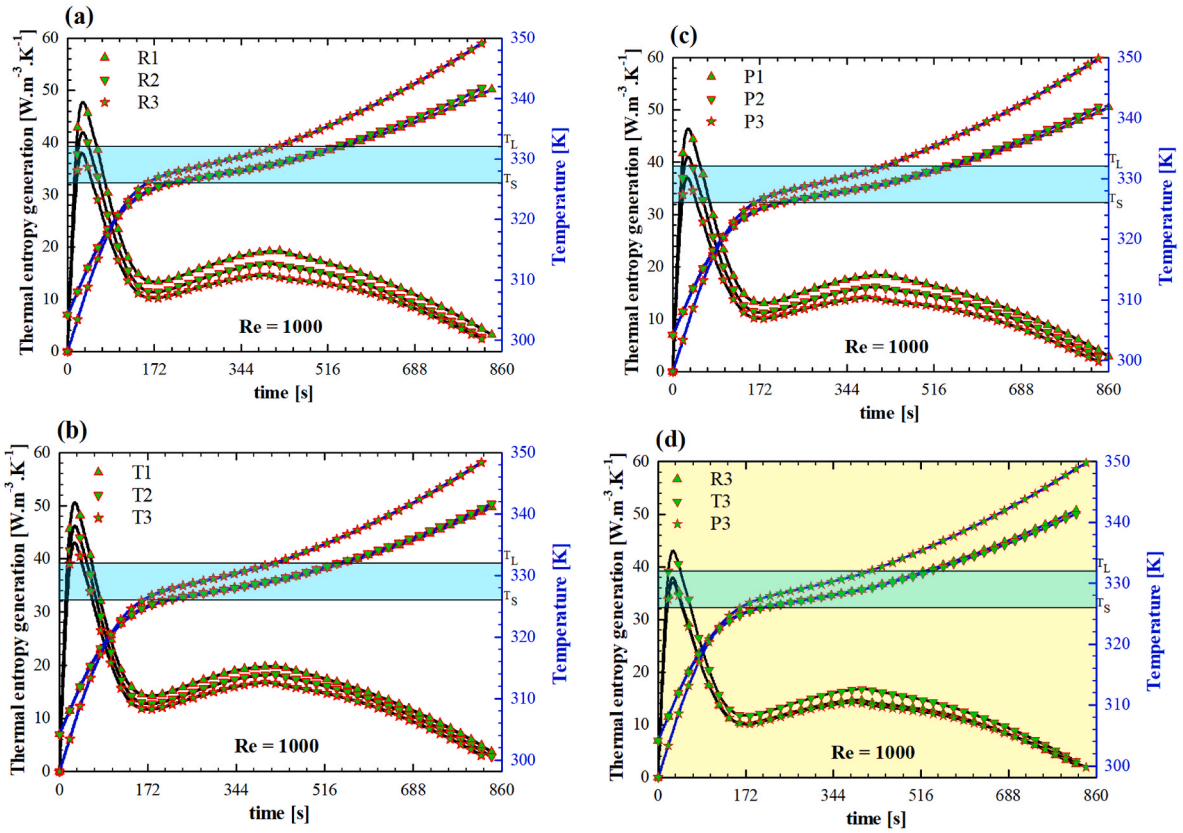

Fig. 10. Time-dependent thermal EnG and average temperature characteristic for PCM melting realized in; (a) rectangular fin geometry, (b) triangular fin geometry, (c) parabolic fin geometry, and (d) best geometries.

in the lower parts of the cavity and become more intense towards the upper points because the melting process is still ongoing. On the other hand, another point that stands out in all geometries and time periods is the high thermal irreversibilities at the tip points of the fins. The reason for this is that while heat is transferred along the fin body, there is a sharper break in the temperature field due to the sudden transition from the fin to the PCM in the tip region. This causes a larger $\partial T/\partial n$ to occur at the tip edge [83]. In addition, the fins also compress the natural convection cells in the molten PCM locally; this produces narrow and steep temperature profiles in the boundary layer, causing the local EnG due to heat transfer to be most pronounced at the fin tips [84–86].

Fig. 12 examines the effect of different fin models on the frictional EnG of PCM. Looking at the results, the general trend observed in all models is that the frictional EnG increases from $t = 0$ until approximately $t = 600$ s due to the onset of natural convection and fluid movement in PCM during the melting process, reaching its maximum value. Then, as the temperature differences in the system decrease, the curves tend to decrease in the time period until the transition to complete melting due to the decrease in natural convection [82]. Increasing fin surface area significantly reduces frictional EnG due to improved flow stability and reduced velocity gradients. Despite the larger contact surface area, the increased heat transfer homogenizes the melting process. This ensures the stability of the natural convection process and suppresses excessive velocity gradients. As a result, viscous dispersion is reduced, leading to lower frictional EnG [85]. This finding demonstrates that proper optimization of fin design can both improve thermal performance and reduce hydrodynamic losses.

When the time-averaged variations in the surface areas of different fin models were examined, it was calculated that the R3 model caused 143% and 63% less frictional EnG compared to the R1 and R2 models, respectively, the T3 model caused 96% and 41% less frictional EnG compared to the T1 and T2 models, respectively, and the P3 model caused 141% and 61% less frictional EnG compared to the P1 and P2 models, respectively. When comparing the widest fin models in Fig. 12 (d), it was found that the numerical value of the P3 model was the lowest, but the difference with the R3 model was not proportionally significant, and it was 29% lower than the T3 model.

Time-dependent frictional EnG contours of models with different fin geometries and surface areas are presented in Fig. 13. It is observed that the changes at $t = 200$ and 400 s parallel the thermal EnG colour changes. As the PCM begins to melt, the high temperature difference in the system causes a decrease in density, triggering the buoyancy force in the cavity and initiating the natural convection effect. Local increases in frictional EnG occur with increasing flow velocity. Examining the changes at $t = 600$ and 800 s, it is seen that the friction-induced irreversibilities tend to rise towards the top of the cavity. This is due to the fact that in the lower region of the cavity near the water inlet, the PCM has completely reached the liquid phase and local temperature changes have been minimized [87,88].

The total EnG results of PCM, calculated according to Eq. (16), follows the same trend as the thermal EnG. This leads to the conclusion that the irreversibilities causing thermal EnG are dominant over the irreversibilities causing frictional EnG, and similar results have been found in studies in the literature [82,83]. The physical mechanism that causes this result can be explained as follows: during PCM melting, frictional EnG is small due to low velocity/laminar flow, whereas thermal EnG is dominant because the melting process is controlled by heat transfer and phase change, forming large temperature gradients and latent heat exchange. The strong temperature gradients that form between the heat transfer fluid and the PCM, especially in the early stages of the melting process, are influential in achieving this result.

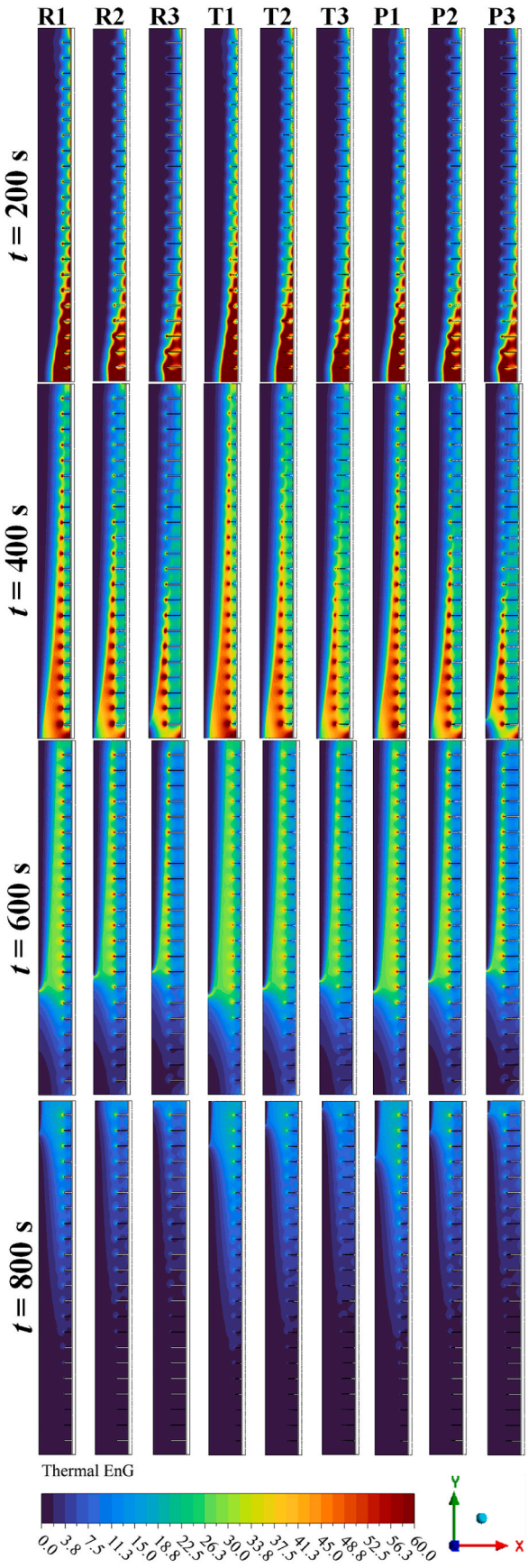

Fig. 11. Time-dependent PCM thermal EnG contours.

3.2. Effect of flow regime

As a result of the investigations carried out in Section 3.1, it was concluded that the P3 model is the most suitable model among all models in terms of energy storage and EnG. In this context, the effect of water flowing through the inner tube at Re = 1000 and 2000 flow regimes on the liquid fraction characteristic, energy storage capacity, and EnG in the PCM is discussed in this section.

In this context, Fig. 14 shows the liquid fraction (left y-axis) and energy storage performance (right y-axis) results for Re = 1000 and 2000 flow regimes. When the liquid fraction results of PCM in LHTES were examined, it was determined that the Re = 2000 state with $\beta = 1$ was reached at $t = 667$ s, which is 156 s earlier compared to Re = 1000. The physical mechanism that enables this is due to the interaction between flow velocity and convective heat transfer [89]. With the increase in flow regime, velocity gradients increase, the thermal boundary layer becomes thinner, and this increases heat transfer between the wall and the fluid, resulting in more heat energy transfer from the high-energy water in the inlet section to the PCM [90]. When the change in energy levels stored in the case of $\beta = 1$ for two different flow regimes is examined, it is calculated that $\Delta H = 264$ kJ kg^{-1} energy is stored at Re = 2000, and $\Delta H = 263$ kJ kg^{-1} energy is stored at Re = 1000. These results show that increasing the flow regime in LHTESs where heat transfer takes place under forced convection conditions is a suitable method in terms of reducing the time difference between the stored energy and the energy demand.

Fig. 15 shows the time-dependent liquid fraction contours of PCM under the influence of water flowing at a laminar flow regime of Re = 1000 and 2000 and $T_{inlet} = 358$ K. Examination of the figures reveals that the increase in flow regime significantly affects the PCM melting process. At Re = 1000, water exhibits weak forced convection, and heat transfer is relatively more limited by conduction mechanisms compared to Re = 2000. In this case, the thermal boundary layer of water is thicker, and the solid-liquid interface of the PCM shows a more chaotic progression along the melt front flow direction. On the other hand, it is observed that the liquid fraction remains lower, especially in the regions between fins or heat transfer surfaces, and local delays occur in melting. This situation is directly related to the limited convective heat transfer coefficient at low flow regimes.

In contrast, as the flow regime increases to Re = 2000, the effect of forced convection is strengthened, and a significant increase in the convective heat transfer coefficient occurs. This situation leads to thinning of the thermal boundary layer of water and more efficient transfer of heat from the wall into the PCM [91]. As a result, the liquid fraction contours show a more homogeneous solid-liquid interface development that progresses faster along the flow direction. On the other hand, it is clearly seen at the same time steps that the PCM melts at a higher rate, and the solid phase disappears in a shorter time at Re = 2000. In addition, at this point, melting starts faster, especially in the inlet region, and a more uniform liquid fraction distribution is observed in the $+y$ direction as time progresses. This result is a clear indication that high flow velocity reduces temperature gradients, creating a more balanced heat transfer process throughout the system.

The influence of Re on EnG characteristics is also examined to evaluate the thermodynamic behaviour of the LHTES. Fig. 16 shows the time-dependent variation of thermal EnG (red) and frictional EnG (blue) in the melting of PCM in the flow regimes of hot water flowing through the inner tube at Re = 1000 and 2000. It is observed that the thermal EnG reaches its peak value for both flow regimes in the initial stage of the melting process (up to $t = 40$ s). The primary reason for this is that temperature gradients are high in the initial stage of the process, and heat transfer occurs primarily through conduction [92,93]. In particular, the fact that the thermal EnG is initially higher in the Re = 2000 flow regime compared to Re = 1000 (35% at $t = 40$ s) is related to the increase in the convective heat transfer coefficient and therefore the occurrence of stronger thermal irreversibilities depending on the

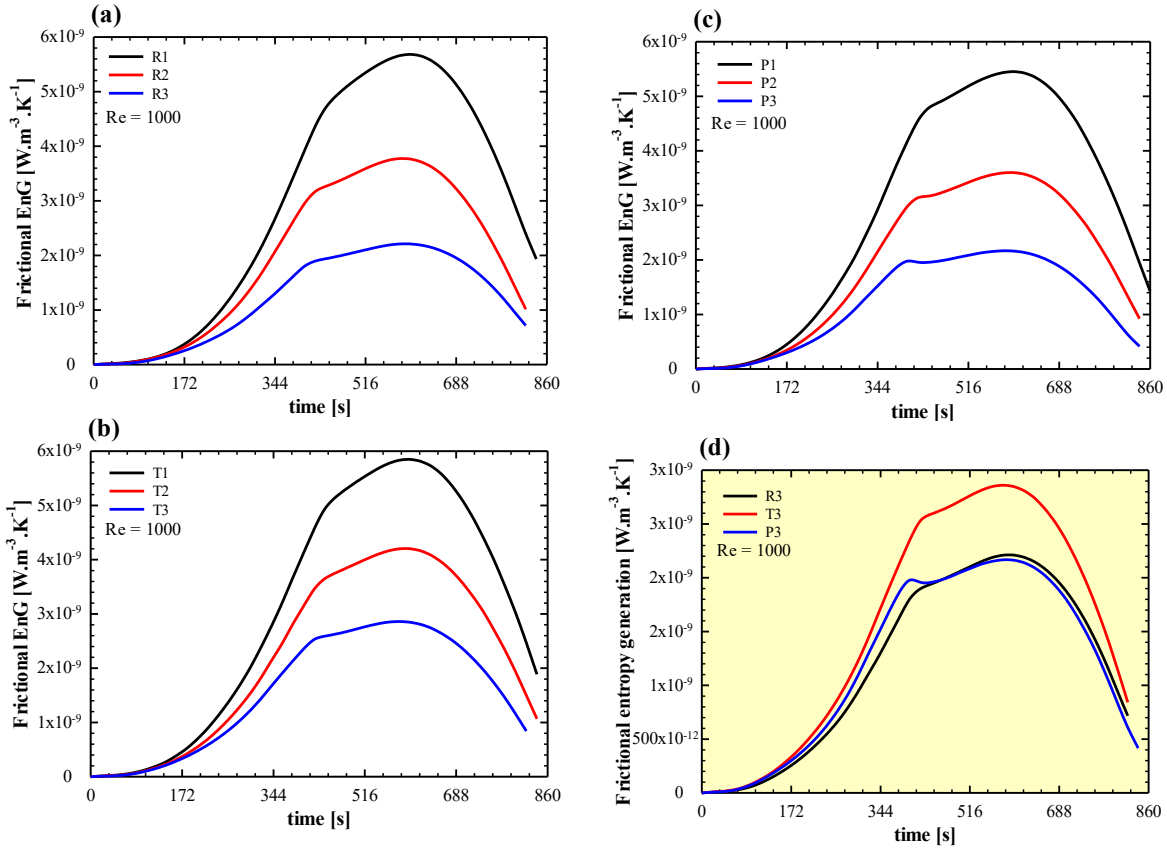

Fig. 12. Time-dependent frictional EnG characteristic for PCM melting realized in; (a) rectangular fin geometry, (b) triangular fin geometry, (c) parabolic fin geometry, and (d) best geometries.

increasing flow regime value [94]. As time progresses, the increase in liquid fraction in the PCM reduces the temperature differences in the cavity, making the heat transfer more homogeneous. This situation results in a steady decrease in thermal EnG in both flow regimes. The fact that this decrease is earlier and more pronounced at Re = 2000 indicates that the high flow regime contributes to the faster melting of the PCM, and the system reaches thermal equilibrium in a shorter time. Therefore, this result provides a characteristic of increasing the heat transfer performance of the system, making the heat storage and discharge cycles in the system more frequent and efficient, and increasing the energy storage efficiency.

Frictional EnG, on the other hand, is initially negligible, but becomes increasingly significant over time and reaches its maximum value at approximately $t = 580$ s at Re = 1000 and at approximately $t = 460$ s at Re = 2000. The main reason for this is that the interaction between the liquid phase and the hot wall increases with the melting of the PCM, and viscous losses in the flow field become increasingly important [95]. As expected, increasing the flow regime significantly increases Frictional EnG. The results obtained at Re = 2000 indicate a higher peak value (58% higher than at Re = 1000), as well as earlier onset, suggesting that viscous irreversibilities, resulting from high velocity gradients and increased shear stresses, have become more dominant. However, the decrease in frictional EnG towards the end of melting can be explained by the system reaching a more thermally and subsequently hydrodynamically stable structure and the weakening of frictional effects in the flow field.

Furthermore, the effect of frictional EnG is significantly smaller than the thermal EnG. This indicates that the dominant source of thermodynamic irreversibility in the current system is related to heat transfer processes rather than friction. Therefore, improving the homogeneity of heat transfer within the PCM space plays a significant role in minimizing total EnG and enhancing the thermodynamic performance of the LHTES. From a second-law perspective, the results show that operating conditions that increase heat transfer while maintaining moderate flow resistance provide more favourable thermodynamic performance by reducing overall irreversibility in the system.

Fig. 17 shows the distributions of thermal EnG and frictional EnG in the PCM melting and storing energy with the help of hot water flowing in the flow regimes of Re = 1000 and 2000 for over time. The presented contours clearly demonstrate the temporal and hydrodynamic dependence of the irreversibilities in the system. Examining Fig. 17(a), it can be seen that increasing the flow regime from Re = 1000 to 2000 visibly affects both the magnitude and local distribution of thermal EnG. In the case of Re = 2000, higher velocity gradients are formed at the wall and PCM interface, the heat transfer coefficient increases, and the temperature gradients become sharper. This situation leads to the formation of high thermal EnG regions, which are concentrated especially on the fin surfaces and in the contact areas between the wall and the PCM. For Re = 1000, the heat transfer in the system remains relatively limited due to the lower velocity and weaker chaotic environment, leading to a lower and more localized thermal energy. Over time, as the liquid fraction of the PCM increases, the effects of natural convection strengthen, the temperature differences between the wall and the PCM decrease. Consequently, the thermal energy exhibits a more homogeneous distribution throughout the cavity.

Fig. 17(b) shows the local variations of frictional EnG during heat interaction between hot water and PCM via wall and fin structures at different times for Re = 1000 and 2000, using contours. It is clearly seen that frictional EnG is concentrated in regions close to the channel walls and fin surfaces. This is directly related to the fact that high velocity gradients ($\partial u/\partial n$) reach their maximum values, especially between the wall and the PCM. In the middle sections of the cavity, however, the

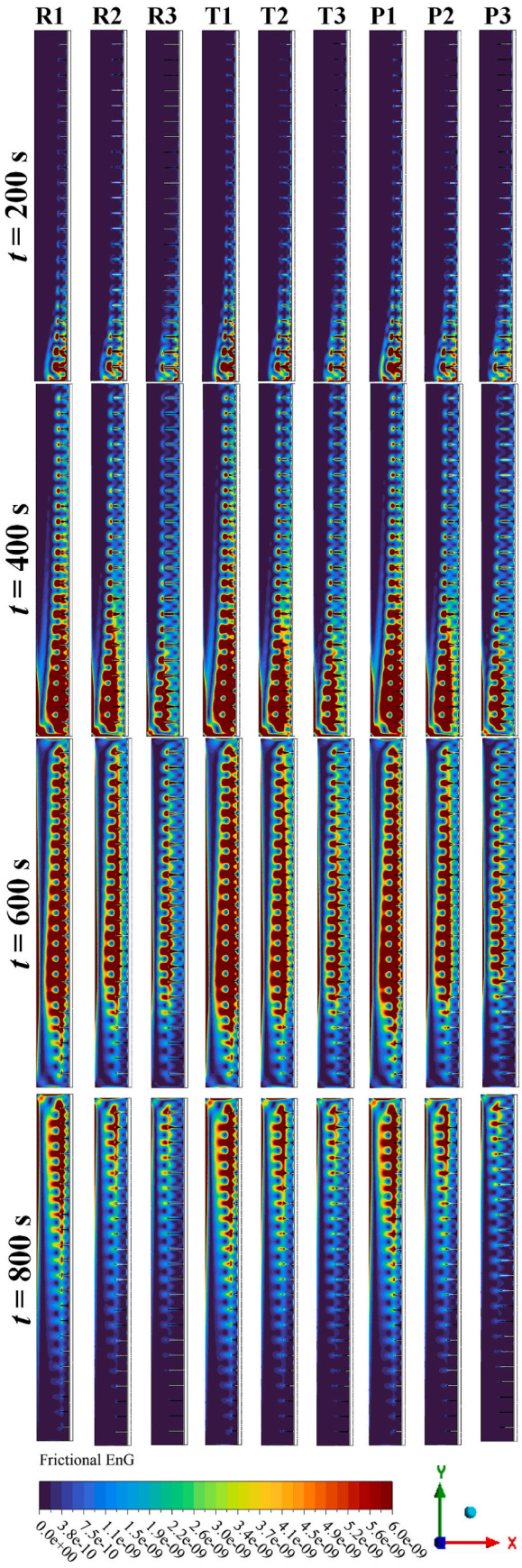

Fig. 13. Time-dependent PCM frictional EnG contours.

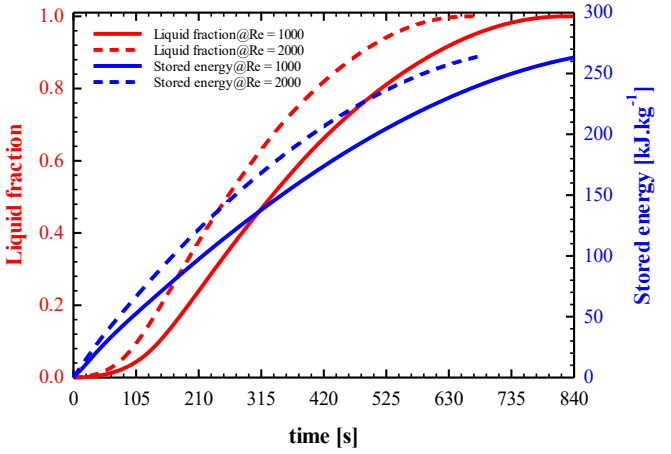

Fig. 14. Variation of liquid fraction (left) and stored energy (right) on condition different laminar flow regime in P3 model as a function of time.

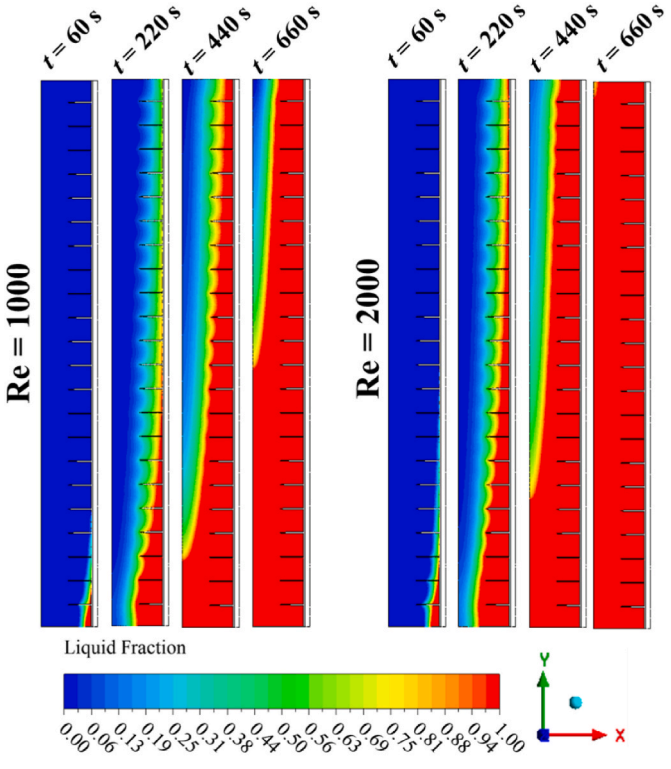

Fig. 15. Effect of Re on PCM melting over time.

irreversibility is negligible because the velocity gradients are limited. This observation indicates that frictional EnG is controlled by a viscous dissipation mechanism. On the other hand, it is clearly observed that higher and more widespread irreversibility occurs at Re = 2000. After the flow regime increases from Re = 1000 to 2000, the velocity gradients near the wall become sharper, and consequently, viscous losses and frictional EnG increase. In the early stages, the flow field is restricted because a large amount of PCM is in the solid phase. In addition, accelerations caused by local temperature changes on the fin also lead to sudden local irreversibilities.

Table 4 presents a quantitative comparison between the current study and previous studies to highlight the performance improvements obtained. However, previous studies did not consider the effect of fin structure or include EnG analysis. In this study, a more comprehensive approach was adopted by comparing different fin structures under equal

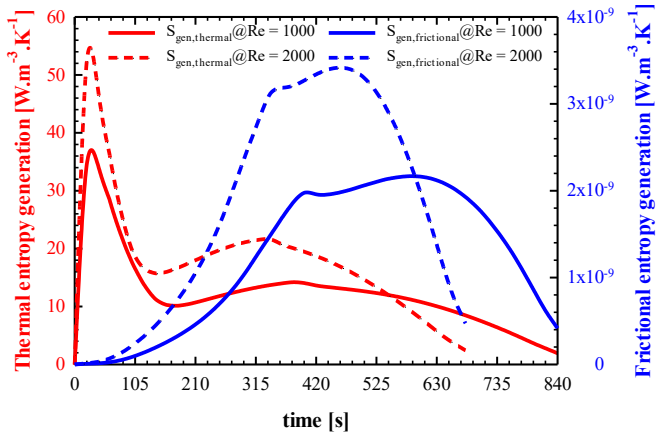

Fig. 16. Variation of thermal EnG (left) and frictional EnG (right) on condition different laminar flow regime in P3 model as a function of time.

surface area conditions and evaluating system performance based on both melting behaviour and EnG. Overall, the findings show that the current study provides a more detailed and balanced evaluation compared to the existing literature.

4. Conclusions

In this study, the melting characteristics, energy storage performance, and EnG of a vertical shell and tube type LHTES system enhanced with MF and fins of different geometries were comprehensively investigated. The results provide a detailed thermo-fluid, energy storage, and second-law assessment of MF-fin hybrid structures, which are rarely addressed together in the literature. The main conclusions obtained from the numerical results are as follows.

- Fin geometry and size have a significant impact on heat transfer and PCM melting time. Although all fin models have the same surface areas, rectangular fins provide the shortest melting time, while parabolic fins ensure a more uniform melting behaviour, indicating their advantage in achieving thermally stable phase change process.
- Model R3 reduced melting time by 0.3% compared to model T3 and by 1.9% compared to model P3. However, this improvement in melting time should be evaluated together with thermodynamic performance, as faster melting does not necessarily correspond to higher system efficiency.
- Increasing the fin surface area consistently enhances heat transfer, shortens melting time, and promotes a more homogeneous liquid fraction distribution. In addition, the longest fin configurations (R3,

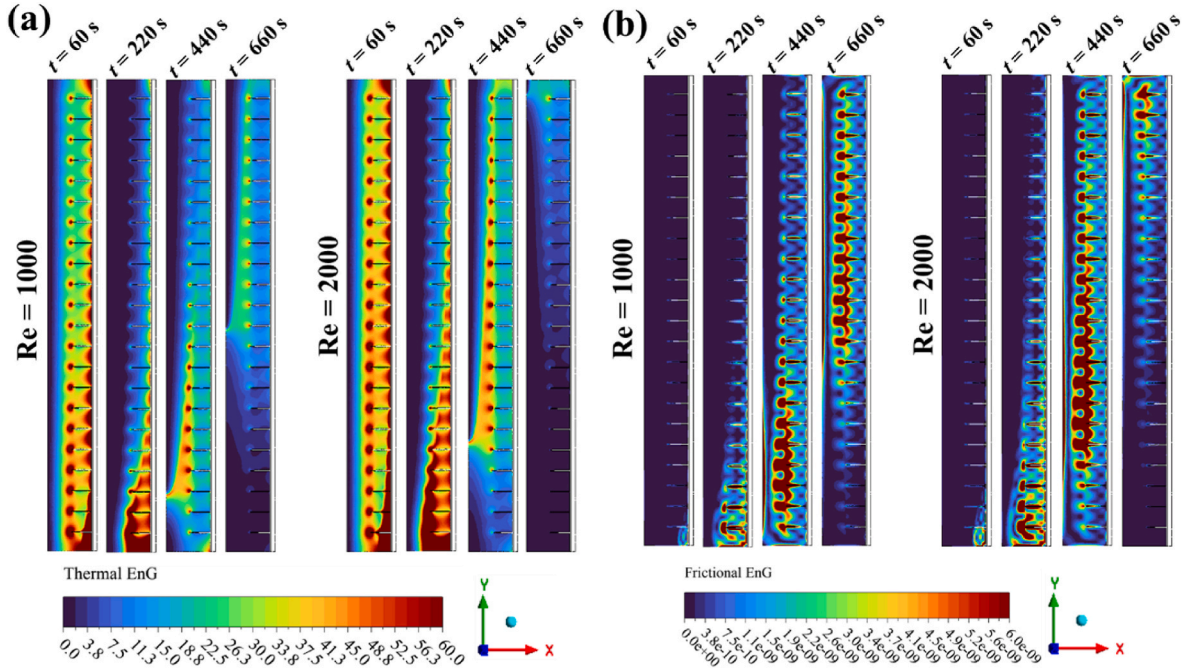

Fig. 17. Effect of Re on PCM melting over time.

Table 4
Comparison of present study results with similar researches.

Study	System type	Enhancement method	Key parameter	Main outcome	Comparison with present study
Lu et al. [33]	Shell and tube	MF + straight fins	Melting time	60% reduction	Present study adds fin geometry optimization + EnG analysis
Mahdi et al. [34]	Shell and tube	MF + straight fins	Melting time	58% (MF) and 42% (fin) reduction	Present study evaluates EnG
Wu et al. [42]	Shell and tube	Annular fins	Heat transfer performance and stored energy	6.17% and 0.43% increment in heat transfer performance and stored energy	Present study investigates MF + fin effect
Present	Vertical shell and tube	MF + fins (rectangular, triangular, parabolic)	Melting time, energy storage, and EnG	Melting time decreased 23%, EnG decreased 19% and more uniform melting provided	First study combining vertical geometry + MF + fin shape comparison + second-law analysis

T3, and P3) significantly reduce both thermal and frictional EnG, indicating improved thermodynamic performance.

- The most thermodynamically optimal configuration was found to be model P3 with parabolic tips, which provides a balanced improvement in melting uniformity, energy storage performance, and EnG. This model exhibited higher second-law efficiency, reducing total EnG by 4% and 19%, respectively, compared to rectangular and triangular fins.
- Another noteworthy aspect of the analysis results is that increasing the fin surface area leads to a significant reduction in frictional EnG in PCM. Model P3 resulted in 141% and 61% less frictional EnG compared to models P1 and P2, respectively. This is attributed to the stabilization of natural convection and suppression of excessive velocity gradients, demonstrating that properly designed fin structures can simultaneously enhance thermal performance and reduce hydrodynamic losses.
- Increasing the flow regime (from Re = 1000 to Re = 2000) strengthened the forced convection effect, reducing the melting time of the PCM by 23%. However, this resulted in high thermal and frictional EnG in the initial stages of melting, indicating a trade-off between heat transfer enhancement and thermodynamic irreversibility.
- A general assessment of the findings reveals that MF-fin hybrid structures have strong potential for developing a high-performance and thermodynamically more efficient vertical shell and tube type LHTES system. In this respect, the analyses provide unique, comprehensive, and guiding results for vertical model systems, which are discussed in a limited number of the literature.
- From an application perspective, the findings of this study provide practical design guidelines for optimizing fin geometry and flow conditions in LHTES systems used in solar energy storage, waste heat recovery, and thermal management applications.
- Finally, the numerical framework and insights presented in this study can serve as a reference for future studies investigating more complex conditions, such as different PCMs, alternative fin configurations, and extended flow regimes including transitional and turbulent flows.

Declaration of competing interest

The authors declare that they have no known competing financial interests or personal relationships that could have appeared to influence the work reported in this paper.

Data availability

The data that has been used is confidential.

References

[1] C. E, Burak Kara, Enerji depolama teknolojilerinin incelenmesi ve Karşılaştırmalı analizi, Int. J. Multidiscip. Stud. Innov. Technol. (2022). https://dergipark.org.tr/tr/pub/ijmsit/issue/73364/1192595.

[2] E. T, Elif Nur Bilen, Hamza Alahmad, GELECEĞİN ENERJİ DEPOLAMA TEKNOLOJİLERİ, SÜRDÜRÜLEBİLİRLİK VE ENERJİ DÖNÜŞÜMÜ, Mühendis Ve Makina, vol. 65, 2024, pp. 1–26, https://doi.org/10.46399/muhendismakina.1460634.

[3] M.K. Asım, Sinan Karakurt İdris Tan Akçay, trends and emerging themes in thermal energy storage: a bibliometric Study, J. Mar. Eng. Technol. 4 (2024) 44–53, https://doi.org/10.58771/joinmet.1584084.

[4] P.B.A.P.Y.P.R.Y, Pramod Kale, Prayas Gondane, Phase change materials in thermal energy storage: a comprehensive review of properties, advances, and challenges, 1st Int. Conf. Sustain. Energy Technol. Comput. Intell. Towar. Sustain. Energy Transition, SETCOM (2025) 2025, https://doi.org/10.1109/SETCOM64758.2025.10932354.

[5] J. L, Su-Gwang Jeong, Taemin Lee, Evaluation of energy performance and thermal comfort considering the heat storage capacity and thermal conductivity of biocomposite phase change materials, Processes 9 (2021) 2191, https://doi.org/10.3390/pr9122191.

[6] Y. B, M.Z. S, M.M. Ismail, I. Dincer, Nanoparticles enhanced phase change materials for thermal energy storage applications: an assessment, Int. J. Thermofluids 27 (2025) 101207, https://doi.org/10.1016/j.ijft.2025.101207.

[7] X. Zhai, Z. Xu, W. Zhang, Q. Zhang, X. Yang, J. Qu, G. Liu, B. Yu, Phase change thermal energy storage: materials and heat transfer enhancement methods, J. Energy Storage 123 (2025) 116778, https://doi.org/10.1016/j.est.2025.116778.

[8] S.M. Borhani, M.J. Hosseini, R. Pakrouh, A.A. Ranjbar, A. Nourian, Performance enhancement of a thermoelectric harvester with a PCM/metal foam composite, Renew. Energy 168 (2021) 1122–1140, https://doi.org/10.1016/j.renene.2021.01.020.

[9] Z. Zhang, N. Zhang, Y. Yuan, W. Jiao, P.E. Phelan, Investigations on transient thermal performance of phase change materials embedded in metal foams for latent heat thermal energy storage, Int. J. Energy Res. 45 (2021) 20763–20782, https://doi.org/10.1002/er.7137.

[10] L. T, L.L. L, W. A, W.Q. Li, S.J. Guo, Heat transfer enhancement of nano-encapsulated phase change material (NEPCM) using metal foam for thermal energy storage, Int. J. Heat Mass Transf. 166 (2021) 120737, https://doi.org/10.1016/j.ijheatmasstransfer.2020.120737.

[11] B. Yang, Y. Cao, R. Zhang, X. Yu, Experimental investigation on the stability and heat transfer enhancement of phase change materials composited with nanoparticles and metal foams, J. Energy Storage 89 (2024) 111826, https://doi.org/10.1016/j.est.2024.111826.

[12] H. Najafi Khaboshan, K. Kadirgama, D. Ramasamy, V. Talele, P. Zhao, H. Tyagi, N. Miljkovic, Thermal uniformity analysis of a hybrid battery pack using integrated phase change material, metal foam, and counterflow minichannels, Appl. Therm. Eng. 259 (2025) 124910, https://doi.org/10.1016/j.applthermaleng.2024.124910.

[13] J. Guo, Z. Du, G. Liu, X. Yang, M.-J. Li, Compression effect of metal foam on melting phase change in a shell-and-tube unit, Appl. Therm. Eng. 206 (2022) 118124, https://doi.org/10.1016/j.applthermaleng.2022.118124.

[14] A.J. C, A. A, I. M, M. G, Mehdi Ghalambaz, Mutabe Aljaghtham, Mathematical modeling of heterogeneous metal foams for phase-change heat transfer enhancement of latent heat thermal energy storage units, Appl. Math. Model. Simul. Comput. Eng. Environ. Syst. 115 (2023) 398–413, https://doi.org/10.1016/j.apm.2022.10.018.

[15] B. Kurşun, M. Balta, K. Karabulut, Exploring the impact of inner and middle channel geometries on the melting rate of PCM-Metal foam composition in a triplex tube heat exchanger, Therm. Sci. Eng. Prog. 51 (2024) 102621, https://doi.org/10.1016/J.TSEP.2024.102621.

[16] M. T, E. G, Emrehan Gursoy, Mehmet Gurdal, Latent heat thermal energy storage: metal foam configuration and deep learning-based process predictions, J. Energy Storage 130 (2025) 117361, https://doi.org/10.1016/j.est.2025.117361.

[17] P.L.J.F.Q.T.J.L, Yan Zhang, Huihui Wang, Heat transfer analysis of phase change materials with metal foams, 2021 22nd Int. Conf. Electron. Packag. Technol. (2021) 1–5, https://doi.org/10.1109/icept52650.2021.9567957.

[18] V.K. Yadav, M. Jee, J. Sarkar, P. Ghosh, Novel metal foam and phase change material integrated multi-tube heat exchanger design for simultaneous charging and discharging, J. Energy Storage 117 (2025) 116109, https://doi.org/10.1016/j.est.2025.116109.

[19] A. Andreozzi, P. Asinari, A. Barletta, V. Bianco, J.A. Bocanegra, P.V. Brandão, B. Buonomo, R. Cappabianca, M. Celli, E. Chiavazzo, P. De Angelis, A. Diani, S. Filippeschi, M. Iasiello, O. Manca, S. Nardini, C. Nonino, L. Rossetto, Heat transfer and thermal energy storage enhancement by foams and nanoparticles, Energies 16 (2023), https://doi.org/10.3390/en16217421.

[20] Y. Li, Z. Niu, X. Huang, X. Gao, X. Yang, B. Sundén, Effect of pore density and filling ratio of metal foam on melting performance in a heat storage tank, Numer. Heat Transf. Part A Appl. 86 (2025) 1577–1600, https://doi.org/10.1080/10407782.2023.2279290.

[21] B.B.L.Z.R.X.H.W.D.Z, W.Q. Li, T.Y. Zhang, Enhanced energy management performances of passive cooling, heat storage and thermoelectric generator by using phase change material saturated in metal foam, Int. J. Therm. Sci. 184 (2023) 107869, https://doi.org/10.1016/j.ijthermalsci.2022.107869.

[22] L.S.L.W.Y.J.L.T.Z.L.G.W.L.Z.Y.Y, Shuai Zhang, Daili Feng, A review of phase change heat transfer in shape-stabilized phase change materials (ss-PCMs) based on porous supports for thermal energy storage, Renew. Sustain. Energy Rev. 135 (2021) 110127, https://doi.org/10.1016/j.rser.2020.110127.

[23] Z. Bian, F. Hou, Y. Bai, Q. Dong, H. Wang, Composited phase change material with hierarchical metal foam for efficient thermal energy management, Appl. Therm. Eng. 236 (2024) 121745, https://doi.org/10.1016/j.applthermaleng.2023.121745.

[24] P. Yan, W. Fan, Y. Yang, H. Ding, A. Arshad, C. Wen, Performance enhancement of phase change materials in triplex-tube latent heat energy storage system using novel fin configurations, Appl. Energy 327 (2022) 120064, https://doi.org/10.1016/j.apenergy.2022.120064.

[25] S. Gao, Y. Ye, Z. Zhang, Y. Zhang, Performance optimization of hydrogen storage reactors based on composite enhancement of fins and metal foam, Int. J. Hydrogen Energy 128 (2025) 464–472, https://doi.org/10.1016/j.ijhydene.2025.04.247.

[26] M.T.E.H.M.M.A.K.A.R.I, Khaoula Nedjem, Abdelghani Laouer, Performance enhancement of triplex tube latent heat storage using fins, metal foam and nanoparticles, Int. Commun. Heat Mass Transf. 139 (2022) 106437, https://doi.org/10.1016/j.icheatmasstransfer.2022.106437.

[27] M.K.R. Varun Joshi, Experimental and numerical assessments of thermal transport in fins and metal foam infused latent heat thermal energy storage systems: a comparative evaluation, Appl. Therm. Eng. 178 (2020) 115518, https://doi.org/10.1016/j.applthermaleng.2020.115518.

[28] G. Liu, Z. Du, T. Xiao, J. Guo, L. Lu, X. Yang, K. Hooman, Design and assessments on a hybrid pin fin-metal foam structure towards enhancing melting heat transfer: an experimental study, Int. J. Therm. Sci. 182 (2022) 107809, https://doi.org/10.1016/j.ijthermalsci.2022.107809.
[29] Y. Li, F. de León, Y. Zhao, L. Yue, Z. Hu, R. Wang, Influence and comprehensive evaluation of porous metal foam filled fins on the performance of power cable surface waste heat recovery thermoelectric power generation device, Therm. Sci. Eng. Prog. 47 (2024) 102278, https://doi.org/10.1016/j.tsep.2023.102278.
[30] P. Samudre, S.V. Kailas, Thermal performance enhancement in open-pore metal foam and foam-fin heat sinks for electronics cooling, Appl. Therm. Eng. 205 (2022) 117885, https://doi.org/10.1016/j.applthermaleng.2021.117885.
[31] Z.N, Chen Ding, Liang Wang, Thermal performance evaluation of latent heat storage systems with plate fin-metal foam hybrid structure, Case Stud. Therm. Eng. (2021), https://doi.org/10.1016/j.csite.2021.101309.
[32] X.H.T.X.X.Y.Y.-L.H, Zhao Du, Gang Liu, Numerical studies on a fin-foam composite structure towards improving melting phase change, Int. J. Heat Mass Transf. 208 (2023) 124076, https://doi.org/10.1016/j.ijheatmasstransfer.2023.124076.
[33] M.W.K.Z.H.X.J.K.H.Y.H.C, Yongwen Lu, Hongyang Zuo, Enhancing the melting performance in latent heat storage systems with fin-foam combination at high temperatures: configurational optimization and economic assessment, Appl. Therm. Eng. 247 (2024) 123036, https://doi.org/10.1016/j.applthermaleng.2024.123036.
[34] I.M.A.A.H.I.M.N.B.K.N.K.A.A.C.P.T, Jasim M. Mahdi, Farqad T. Najim, Intensifying the thermal response of PCM via fin-assisted foam strips in the shell-and-tube heat storage system, J. Energy Storage 45 (2022) 103733, https://doi.org/10.1016/j.est.2021.103733.
[35] B.A.G, Kin Yuen Leong, Syafawati Hasbi, State of art review on the solidification and melting characteristics of phase change material in triplex-tube thermal energy storage, J. Energy Storage 41 (2021) 102932, https://doi.org/10.1016/j.est.2021.102932.
[36] M.F.K. Oudaoui, Numerical study of latent heat discharge of a phase change material shell-and-tube thermal energy storage system, Lect. Notes Mech. Eng (2024) 151–159, https://doi.org/10.1007/978-3-031-46973-2_14.
[37] B.M.S.G.P.J.A.A.S.J, Badal Kudachi, Nilesh Varkute, Experimental and computational study of phase change material based shell and tube heat exchanger for energy storage, Mater. Today Proc. 46 (2021) 10015–10021, https://doi.org/10.1016/j.matpr.2021.05.295.
[38] P.D.P.K.S.P, Debasree Ghosh, Joyjeet Ghose, Strategies for phase change material application in latent heat thermal energy storage enhancement: status and prospect, J. Energy Storage 53 (2022) 105179, https://doi.org/10.1016/j.est.2022.105179.
[39] M.K. Das, Subhakanta Moharana, Anirban Bhattacharya, A critical review of parameters governing the boiling characteristics of tube bundle on shell side of two-phase shell and tube heat exchangers, Therm. Sci. Eng. Prog. 29 (2022) 101220, https://doi.org/10.1016/j.tsep.2022.101220.
[40] E.B.M.R.M.R, Alan Strunga, Tereza Kroulíková, Experimental determination of the heat transfer coefficients of shell-and-tube heat exchangers with different hollow fiber arrangements, J. Therm. Anal. Calorim. 147 (2022) 14787–14796, https://doi.org/10.1007/s10973-022-11576-1.
[41] K.S. Jerzy Wołoszyn, A combined heat transfer enhancement technique for shell-and-tube latent heat thermal energy storage, Renew. Energy 202 (2022) 1342–1356, https://doi.org/10.1016/j.renene.2022.12.010.
[42] R.Y.A.M.C.L, Yangyang Wu, Dong Li, Enhancing heat transfer and energy storage performance of shell-and-tube latent heat thermal energy storage unit with unequal-length fins, J. Therm. Sci. 32 (2022) 2018–2031, https://doi.org/10.1007/s11630-022-1655-0.
[43] F.B.M.H.A.A.E.B.-H.J.Y.B, Atef Chibani, Slimane Merouani, A strategy for enhancing heat transfer in phase change material-based latent thermal energy storage unit via nano-oxides addition: a study applied to a shell-and-tube heat exchanger, J. Environ. Chem. Eng. 9 (2021) 106744, https://doi.org/10.1016/j.jece.2021.106744.
[44] T.L. Qianjun Mao Kaili Chen, Heat transfer performance of a phase-change material in a rectangular shell-tube energy storage tank, Appl. Therm. Eng. 215 (2022) 118937, https://doi.org/10.1016/j.applthermaleng.2022.118937.
[45] I. Vogeler, R. Cichota, S. Langer, S. Thomas, D. Ekanayake, A. Werner, Simulating water and nitrogen runoff with APSIM, Soil Tillage Res. 227 (2023) 105593, https://doi.org/10.1016/j.still.2022.105593.
[46] M. Yu, X. Zheng, J. Liu, D. Niu, H. Liu, H. Gao, Numerical simulation study of heat transfer fluid boiling effects on phase change material in latent heat thermal energy storage units, Energies 18 (2025), https://doi.org/10.3390/en18143836.
[47] J. Guo, B. Yang, Y. Li, X. Yang, Y.-L. He, B. Sundén, Thermal energy storage characteristics of finned tubes with different gradients of fin heights, Numer. Heat Transf. Part A Appl. 85 (2024) 845–874, https://doi.org/10.1080/10407782.2023.2193707.
[48] N. Ben Khedher, H. Togun, A.M. Abed, H.I. Mohammed, J.M. Mahdi, R.K. Ibrahem, W. Yaïci, P. Talebizadehsardari, A. Keshmiri, Comprehensive analysis of melting enhancement by circular Y-shaped fins in a vertical shell-and-tube heat storage system, Eng. Appl. Comput. Fluid Mech. 17 (2023) 2227682, https://doi.org/10.1080/19942060.2023.2227682.
[49] D.S. Mehta, B. Vaghela, M.K. Rathod, J. Banerjee, Thermal performance augmentation in latent heat storage unit using spiral fin: an experimental analysis, J. Energy Storage 31 (2020) 101776, https://doi.org/10.1016/j.est.2020.101776.
[50] J. Vogel, M. Johnson, Natural convection during melting in vertical finned tube latent thermal energy storage systems, Appl. Energy 246 (2019) 38–52, https://doi.org/10.1016/j.apenergy.2019.04.011.
[51] S.A. Khan, H.E. Abdellatif, Z. Wang, H. Liu, A. Belaadi, A. Alhushaybari, Investigation and optimization of shell-and-tube thermal energy storage unit with biomimetic leaf-vein fins and carbon nanotubes for superior PCM efficiency, Int. Commun. Heat Mass Transf. 167 (2025) 109250, https://doi.org/10.1016/j.icheatmasstransfer.2025.109250.
[52] J. Wang, S.A. Khan, M. Imran, H.E. Abdellatif, U. Farooq, A.M. Alharthi, A. Belaadi, Computational investigation of melting performance enhancement in PCM-based lobed triplex-tube heat exchangers with Y-shaped fins for solar thermal energy storage, Int. Commun. Heat Mass Transf. 169 (2025) 109567, https://doi.org/10.1016/j.icheatmasstransfer.2025.109567.
[53] Y.A. Çengel, A.J. Ghajar, Heat and Mass Transfer Fundamentals & Applications, 2015.
[54] E. Gürsoy, Melting and energy storage performance enhancement of rectangular cavity with metal foam by nano-PCM and recessed/protruding dimpled fin wall, J. Energy Storage 119 (2025) 116327, https://doi.org/10.1016/j.est.2025.116327.
[55] E. Gürsoy, H.K. Pazarlioğlu, M. Gürdal, E. Gedik, K. Arslan, A. Dağdeviren, Investigation of magneto-convection characteristics in a sudden expanding channel with convex surface geometry under thermally developing flow conditions, Int. J. Numer. Methods Heat Fluid Flow (2024), https://doi.org/10.1108/HFF-11-2023-0703.
[56] E. Gürsoy, M. Gürdal, M. Tan, E. Gedik, Latent heat thermal energy storage: metal foam configuration and deep learning-based process predictions, J. Energy Storage 130 (2025) 117361, https://doi.org/10.1016/j.est.2025.117361.
[57] A. Abhat, Low temperature latent heat thermal energy storage: heat storage materials, Sol. Energy 30 (1983) 313–332, https://doi.org/10.1016/0038-092X(83)90186-X.
[58] T. Fiedler, N. Movahedi, Compact aluminium foam heat exchangers, Metals 13 (2023), https://doi.org/10.3390/met13081440.
[59] K. Vafai, S.J. Kim, On the limitations of the brinkman-forchheimer-extended darcy equation, Int. J. Heat Fluid Flow 16 (1995) 11–15, https://doi.org/10.1016/0142-727X(94)00002-T.
[60] X. Yang, S. Feng, Q. Zhang, Y. Chai, L. Jin, T.J. Lu, The role of porous metal foam on the unidirectional solidification of saturating fluid for cold storage, Appl. Energy 194 (2017) 508–521, https://doi.org/10.1016/j.apenergy.2016.09.050.
[61] S. Feng, M. Shi, Y. Li, T.J. Lu, Pore-scale and volume-averaged numerical simulations of melting phase change heat transfer in finned metal foam, Int. J. Heat Mass Transf. 90 (2015) 838–847, https://doi.org/10.1016/j.ijheatmasstransfer.2015.06.088.
[62] B. Buonomo, O. Manca, S. Nardini, R.E. Plomitallo, Numerical study on latent heat thermal energy storage system with PCM partially filled with aluminum foam in local thermal equilibrium, Renew. Energy 195 (2022) 1368–1380, https://doi.org/10.1016/J.RENENE.2022.06.122.
[63] Q. Ying, H. Wang, E. Lichtfouse, Numerical simulation on thermal behavior of partially filled metal foam composite phase change materials, Appl. Therm. Eng. 229 (2023) 120573, https://doi.org/10.1016/j.applthermaleng.2023.120573.
[64] S. Sabet, B. Buonomo, M.A. Sheremet, O. Manca, Numerical investigation of melting process for phase change material (PCM) embedded in metal foam structures with kelvin cells at pore scale level, Int. J. Heat Mass Transf. 214 (2023) 124440, https://doi.org/10.1016/j.ijheatmasstransfer.2023.124440.
[65] H. Kuang, B. Wu, J. Wang, J. Fu, Y. Feng, C. Yu, Z. Wang, J. Zhang, Y. Ji, Wettability and thermal contact resistance of thermal interface material composited by gallium-based liquid metal on copper foam, Int. J. Heat Mass Transf. 199 (2022) 123444, https://doi.org/10.1016/j.ijheatmasstransfer.2022.123444.
[66] L. Chen, A. Fan, Effects of shell modifications and operational parameters on melting uniformity of a vertical multi-section shell-and-tube latent heat thermal energy storage unit, J. Energy Storage 55 (2022) 105593, https://doi.org/10.1016/j.est.2022.105593.
[67] M. Fadl, P.C. Eames, Numerical investigation of the influence of mushy zone parameter Amush on heat transfer characteristics in vertically and horizontally oriented thermal energy storage systems, Appl. Therm. Eng. 151 (2019) 90–99, https://doi.org/10.1016/j.applthermaleng.2019.01.102.
[68] H.K. Pazarlioğlu, E. Gürsoy, M. Gürdal, Z. Said, A.K. Arslan, E. Gedik, Numerical simulation of sudden expansion tubes with Ag-MgO nanofluid and innovative fin structure: a thermo-fluidic analysis, Int. J. Heat Fluid Flow 108 (2024), https://doi.org/10.1016/j.ijheatfluidflow.2024.109448.
[69] A. Bhattacharya, V.V. Calmidi, R.L. Mahajan, Thermophysical properties of high porosity metal foams, Int. J. Heat Mass Transf. 45 (2002) 1017–1031, https://doi.org/10.1016/S0017-9310(01)00220-4.
[70] K. Boomsma, D. Poulikakos, On the effective thermal conductivity of a three-dimensionally structured fluid-saturated metal foam, Int. J. Heat Mass Transf. 44 (2001) 827–836, https://doi.org/10.1016/S0017-9310(00)00123-X.
[71] P.J. Roache, Computational fluid dynamics, Comput. Fluid Dyn (1976).
[72] A. Seeni, P. Rajendran, M. Hussin, F. Ismail, Errors and uncertainties in simulation of steady, viscous flow past a circular cylinder at Re= 20 using a systematic approach, Incas Bull 12 (2020) 203–217, https://doi.org/10.13111/2066-8201.2020.12.3.17.
[73] A. Ibraheem, Evaluating the efficiency of polyhedral mesh elements in solving the problem of the flow around ship's rudder, Int. J. Eng. Manag. Sci. 6 (2021) 241–256, https://doi.org/10.21791/IJEMS.2021.2.21.
[74] Y. Yao, H. Wu, Thermal transport process of metal foam/paraffin composite (MFPC) with solid-liquid phase change: an experimental study, Appl. Therm. Eng. 179 (2020) 115668, https://doi.org/10.1016/j.applthermaleng.2020.115668.
[75] S.A. Marzouk, A. Aljabr, F.A. Almehmadi, M.A. Sharaf, T. Alam, D. Dobrotă, Thermal performance enhancement of phase change material melting using innovative fins, Therm. Sci. Eng. Prog. 61 (2025) 103585, https://doi.org/10.1016/j.tsep.2025.103585.

[76] H. Li, C. Hu, Y. He, D. Tang, K. Wang, Influence of fin parameters on the melting behavior in a horizontal shell-and-tube latent heat storage unit with longitudinal fins, J. Energy Storage 34 (2021) 102230, https://doi.org/10.1016/j.est.2020.102230.
[77] V. Safari, B. Kamkari, N. Hewitt, K. Hooman, Experimental comparative study on thermal performance of latent heat storage tanks with pin, perforated, and rectangular fins at different orientations, Therm. Sci. Eng. Prog. 48 (2024) 102401, https://doi.org/10.1016/j.tsep.2024.102401.
[78] R. De Césaro Oliveski, F. Becker, L.A.O. Rocha, C. Biserni, G.E.S. Eberhardt, Design of fin structures for phase change material (PCM) melting process in rectangular cavities, J. Energy Storage 35 (2021) 102337, https://doi.org/10.1016/j.est.2021.102337.
[79] Y.-Z. Zhu, Y. Huang, L. Zhang, Y.-R. Li, A heat transfer correlation of poiseuille-rayleigh-bénard convection in the thermal entrance region of a horizontal rectangular channel, Case Stud. Therm. Eng. 55 (2024) 104201, https://doi.org/10.1016/j.csite.2024.104201.
[80] H. Ma, B. He, L. Su, D. He, Heat transfer enhancement of nanofluid flow at the entry region of microtubes, Int. J. Therm. Sci. 184 (2023) 107944, https://doi.org/10.1016/j.ijthermalsci.2022.107944.
[81] H.A. Al-Salami, N.S. Dhaidan, H.H. Abbas, F.N. Al-Mousawi, R.Z. Homod, Review of PCM charging in latent heat thermal energy storage systems with fins, Therm. Sci. Eng. Prog. 51 (2024) 102640, https://doi.org/10.1016/j.tsep.2024.102640.
[82] A. Shahsavar, A.H. Majidzadeh, R.B. Mahani, P. Talebizadehsardari, Entropy and thermal performance analysis of PCM melting and solidification mechanisms in a wavy channel triplex-tube heat exchanger, Renew. Energy 165 (2021) 52–72, https://doi.org/10.1016/j.renene.2020.11.074.
[83] A. Shahsavar, A. Goodarzi, I. Baniasad Askari, M. Jamei, M. Karbasi, M. Afrand, The entropy generation analysis of the influence of using fins with tip clearance on the thermal management of the batteries with phase change material: application a new gradient-based ensemble machine learning approach, Eng. Anal. Bound. Elem. 140 (2022) 432–446, https://doi.org/10.1016/j.enganabound.2022.04.024.
[84] M.E. Nakhchi, J.A. Esfahani, Improving the melting performance of PCM thermal energy storage with novel stepped fins, J. Energy Storage 30 (2020) 101424, https://doi.org/10.1016/j.est.2020.101424.
[85] A. Tavakoli, M. Farzaneh-Gord, A. Ebrahimi-Moghadam, Using internal sinusoidal fins and phase change material for performance enhancement of thermal energy storage systems: heat transfer and entropy generation analyses, Renew. Energy 205 (2023) 222–237, https://doi.org/10.1016/j.renene.2023.01.074.
[86] Q. Chen, J. Wu, K. Sun, Y. Zhang, Numerical study of heat transfer enhancement by arc-shaped fins in a shell-tube thermal energy storage unit, Energies 15 (2022), https://doi.org/10.3390/en15207799.
[87] S.S. Mendu, D. Nagaraju, Minimization of entropy generation in natural convection using optimum isothermal heaters: CFD analysis, Int. J. Environ. Sci. Technol. 20 (2023) 5629–5642, https://doi.org/10.1007/s13762-022-04198-5.
[88] B.R. Behera, V. Chandrakar, A. Mukherjee, J.R. Senapati, Entropy production analysis and cooling time calculation for an open hemispherical cavity in natural convection, Proc. Inst. Mech. Eng. Part E J. Process Mech. Eng. 237 (2023) 1249–1261, https://doi.org/10.1177/09544089221117142.
[89] Modeling heat and mass transfer in laminar forced convection in a vertical channel: influence of reynolds number, Phys. Sci. Int. J. 28 (2024) 48–61, https://doi.org/10.9734/psij/2024/v28i5847.
[90] L. Su, Z. Duan, B. He, H. Ma, X. Ning, G. Ding, Y. Cao, Heat transfer characteristics of thermally developing flow in rectangular microchannels with constant wall temperature, Int. J. Therm. Sci. 155 (2020) 106412, https://doi.org/10.1016/j.ijthermalsci.2020.106412.
[91] C. Ozalp, D.B. Saydam, C. Polat, M. Soyler, E. Hürdoğan, An experimental investigation of the flow characteristics and heat transfer properties of a heated and an unheated vertically positioned circular cylinder at different reynolds numbers, Int. J. Heat Mass Transf. 201 (2023) 123637, https://doi.org/10.1016/j.ijheatmasstransfer.2022.123637.
[92] B. Li, R.D. Selvakumar, A.K. Alkaabi, J. Wu, Dynamics of PCM melting driven by spatially varying heat load, Int. Commun. Heat Mass Transf. 157 (2024) 107735, https://doi.org/10.1016/j.icheatmasstransfer.2024.107735.
[93] B. Kiyak, H.F. Oztop, N. Biswas, F. Selimefendigil, Thermal behavior of phase change material in open cavities: effects of opening position and occupancy level, Therm. Sci. Eng. Prog. 62 (2025) 103578, https://doi.org/10.1016/j.tsep.2025.103578.
[94] R. Akhter, M.M. Ali, M.A. Alim, Data analysis of thermal performance and irreversibility of convective flow in porous-wavy channel having triangular obstacle under magnetic field effect, Heliyon 10 (2024) e34580, https://doi.org/10.1016/j.heliyon.2024.e34580.
[95] T. Hayat, K. Muhammad, S. Momani, Melting heat and viscous dissipation in flow of hybrid nanomaterial: a numerical study via finite difference method, J. Therm. Anal. Calorim. 147 (2022) 6393–6401, https://doi.org/10.1007/s10973-021-10944-7.